The Role of Dolomite Content on the Mechanical Strength and Failure Mechanisms in Dolomite-Limestone Composites

by

Nathan R. Cleven

A THESIS SUBMITTED IN PARTIAL FULFILLMENT OF
THE REQUIREMENTS FOR THE DEGREE OF
BACHELOR OF SCIENCE

In

THE FACULTY OF SCIENCE
Department of Earth and Ocean Sciences

This thesis conforms to the required standard

.....
Supervisor

THE UNIVERSITY OF BRITISH COLUMBIA MARCH 2008

Contents

List of Figures

List of Tables

1 Abstract

Variably dolomitized limestone samples from the Rundle Group in Western Alberta, Canada were deformed under a variety of confining pressures and at room temperature in a triaxial rock press. The aim of this research is to establish the mechanical behaviour and brittle constitutive laws of limestone and dolomite composites. This data can then be used to develop strength profiles of thrust faults in the Rocky Mountain Fold and Thrust Belt. For example, many of the thrust faults in the Canadian Foreland are composed of limestone–dolomite composites, yet the mechanical properties of these composites remain unknown. Sample protoliths were selected for their similar grain sizes and grain size distributions, low porosity and low silica content in order to best examine relationships between these parameters and the distribution of strain between the dolomite and calcite.

This study shows that increasing dolomite content correlates to an increase in strength at low and medium confining pressures. At high confining pressures, distributed brittle deformation adds complexities that are attributed to textural controls. Microstructural analysis of deformed samples shows that at approximately thirty to forty-five weight percent dolomite is interconnected via a dolomite grain network that provides a load-bearing capacity to the dolomite. This load-bearing capacity correlates to dramatic jumps in the strength of dolomite–limestone composites observed with increasing confining pressures.

Inherent weaknesses in calcite grains such as twin planes and cleavage intersections are exploited by fractures resulting in reduced peak strengths of calcite-rich composites. Calcite generally absorbs strain and distributes it into finer spaced fracture networks than in dolomite. In dolomitized rock that still contains calcite cleavage within dolomite is not exploited, rather transgranular cracks break dolomite down into irregular and angular particles. At near pure dolomite content and at high confining pressure dolomite will fracture and disaggregate along cleavage. Comminuted dolomite grains commonly show a larger distribution of sizes and have more irregu-

lar shapes than contiguous comminuted calcite grains. Comminuted calcite particles are commonly much smaller than comminuted dolomite grains and show more regular shapes and an even grain size distribution.

2 Introduction

Calcite and dolomite are chemically and structurally similar, yet dolomite is significantly stronger than calcite. Calcite can deform plastically at room temperature and moderate confining pressures whereas dolomite remains brittle and very strong, especially at high confining pressures. In variably dolomitized rocks, the enrichment of dolomite may increase the strength of limestone rocks. Mechanical strengths of single crystal calcite [4],[10], limestone and marble [11] are well documented and some work exists concerning the deformation of metamorphic dolomite [1], [8]. In contrast, quantification of the effect of adding dolomite to limestone has not been studied. This data would be useful in quantifying the strength of carbonate thrusts in the Foreland of the Canadian Rockies where much of the limestone is variably dolomitized.

Other bimineralic systems, however, have been studied. For example synthetic calcite – anhydrite aggregates demonstrate that straying from end-member compositions causes complex deformation mechanisms involving strain localization to specific phases [2]. In addition, experiments with quartz in clay gouge demonstrate that the moderate quartz compositions would create load-bearing grain networks increasing the frictional sliding strength of the experimental fault gouge [7]. It is hypothesized that dolomitization would largely control failure mechanics through the spatial distribution of dolomite grains amongst the calcite. A threshold of dolomite content providing an interconnected grain support network will induce strain partitioning into the stronger mineral [5], [9]and cause an escalation of peak strength and the capacity to elastically deform. The aim of this research is therefore to deform natural variably dolomitized rock samples in a triaxial press to experimentally derive the mechanical data to quantify this threshold. The key focus of the results will be the microstructural analysis to examine how the natural textures and grain structures of dolomitized limestone rocks influence the brittle deformation mechanisms.

3 Methodology

3.1 Starting Material

The regions around Crowsnest Pass and Canmore, Alberta, were targets for sampling. Samples were selected and sampled from outcrop and fresh quarry rubble based on their visible grain size and approximate dolomite content. Low porosity samples were desired to minimize the deformation mechanisms associated with closing porosity during experimental deformation. A consistent grain size between samples was desired but was found only to a degree. Most samples consist of a micritic fraction of ground mass with the rest as fine sub-millimeter mineral grains with a small proportion of larger grains supported by the finer matrix elements. With increasing dolomite percent micrite and smaller calcite grains are preferentially replaced by well-formed small dolomite crystals, increasing in size as the rock nears full dolomite replacement.

A summary of sample measurements is presented in Table 1 and statistical calculations relevant to each sample type in Table 3.

3.1.1 Loomis Member – 3% Dolomite

The Loomis Member sample provides the near pure limestone end-member. In hand sample it is a fine grained grey matrix-supported rock with visible millimeter sized calcite crystals and fossil fragments. Pycnometry measurements indicate an average porosity among sample cores of 0.5%. Thin section characterization (Figure 1 A) gives grain size data in Table 5 with an approximate composition of 65% micrite and 35% grains, giving the thin section a dark brown colour. The grain size of the micrite are in the $10\mu m$ and smaller scale from thin section and SEM backscatter imaging. The majority of observed crystals are anhedral. The grains making up the main population of crystals are fairly equant, but larger millimeter scale grains are often long and thin, with an approximate $3:1$ length:width ratio.

Calcite twins in two opposing cleavage orientations, appears with a $20-30\mu m$ spacing. Grain

boundaries are diffuse, irregular and seem damaged or dissolved in most grains and infilled with micrite.

3.1.2 Salter Member – 31% Dolomite

The Salter Member sample provides the first of a series of three dolomitic limestones of fairly similar compositions but different textures. Hand samples appear light brown-grey on fresh rock, and light grey on weathered surfaces. Pycnometry measurements indicate an average porosity among sample cores of 0.2%. Thin section characterization (Figure 1 B) and SEM images show compositions of 40% micrite and 60% grains, with the micrite grains smaller than the $10\mu m$ scale. Thin sections exhibit a smaller average grain size than Loomis 3% (Table 5) and fine-grained dolomite is evenly distributed (Figure 3 A). The dolomite grains are equant and euhedral and are largely supported in the micritic matrix. Calcite grains show twins in two opposing cleavage orientations, on the 15 to $35\mu m$ scale. Grain boundaries are sharp and irregular.

3.1.3 Loomis Member – 34% Dolomite

The Loomis Member sample is grey with a dolomite composition comparable to the Salter Member 31%. The grain sizes, shapes, distributions, as well as the micrite to grain composition are comparable to the Loomis Member 3% dolomite. Pycnometry measurements indicate an average porosity among sample cores of 0.4%. Thin section characterization (Figure 1 B) shows an approximate 45% composition of micrite sized grains and 55% composition of dolomite and calcite grains. Calcite grains are twinned in two orientations approximately spaced on a $20\mu m$ scale. Sub-millimeter scale fossil fragments are present, some oval-shaped structures with rotary extinction. Because of the larger calcite crystals dolomite distribution is spatially restricted and, in patches, is sufficiently densely distributed to support each other for multi-millimeter lengths (Figure 3 B). Calcite grain boundaries are diffuse and irregular. Dolomite grains are small and usually euhedral.

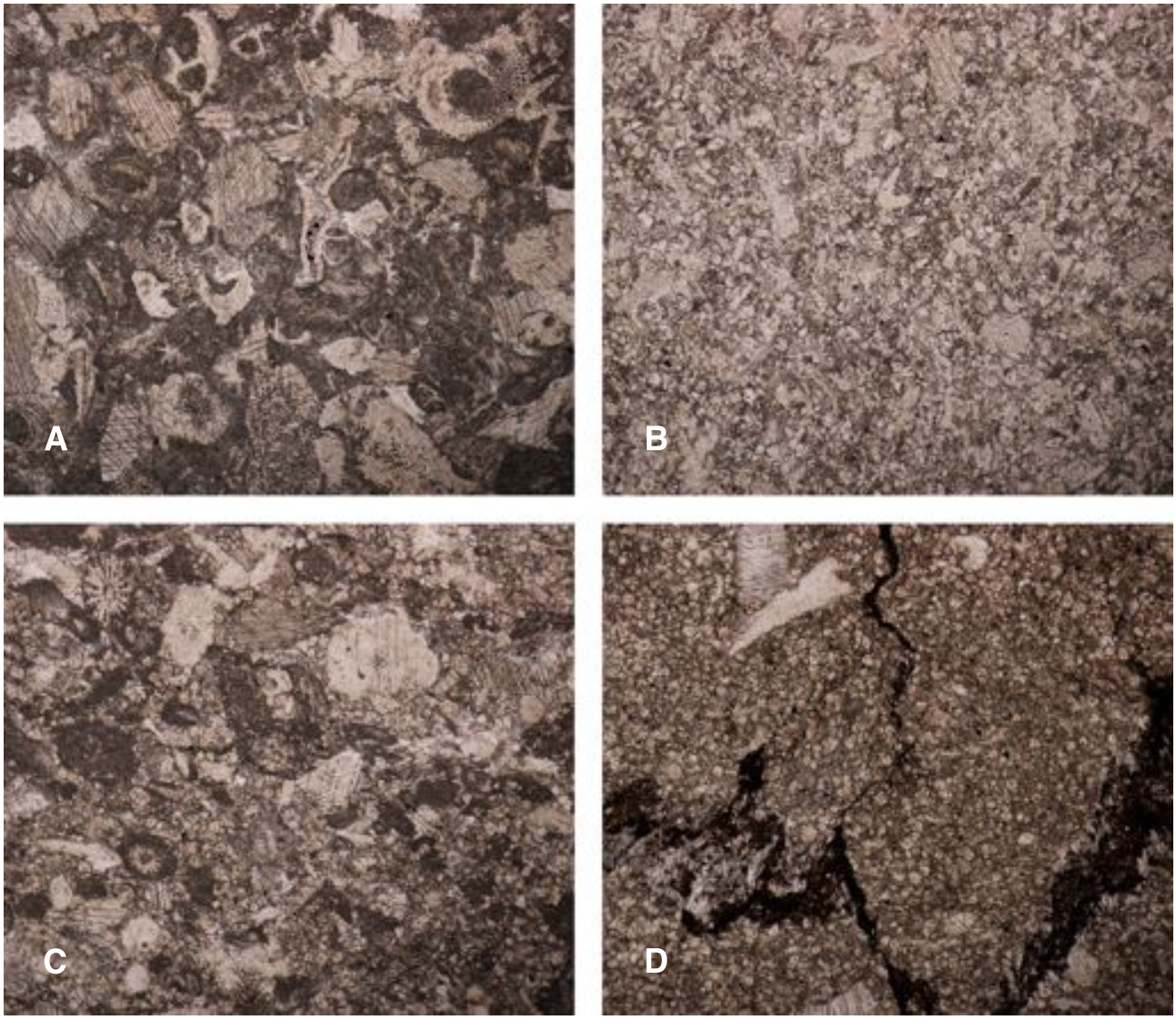

Figure 1: Protoliths in thin-section (PPL). *All fields of view are 3mm across.* **A** Loomis Member 3%. **B** Salter Member 31%. **C** Loomis Member 34%. **D** Loomis Member 43%.

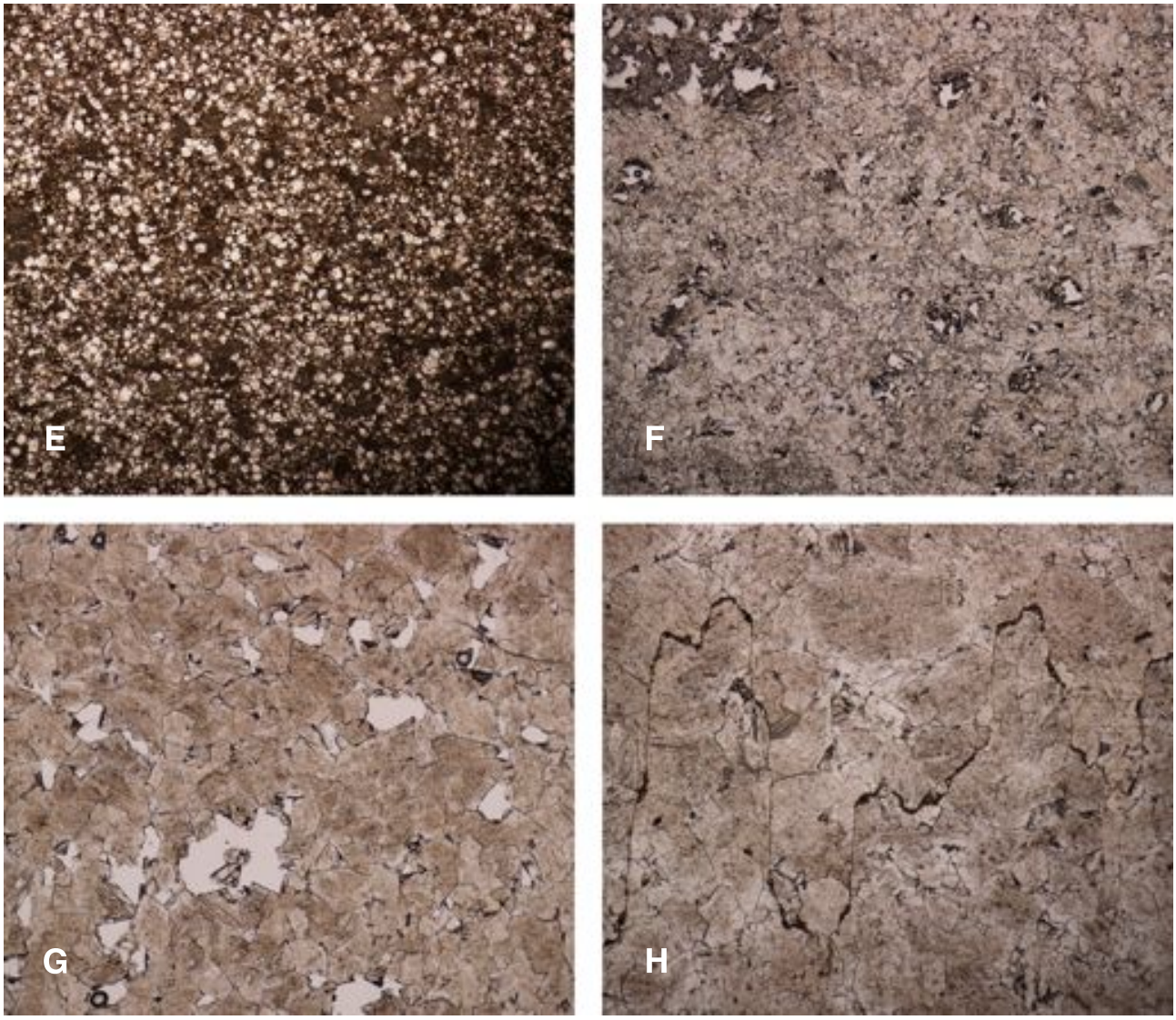

Figure 2: Protoliths in thin-section (PPL). *All fields of view are 3mm across.* **E** Opal Member 48%. **F** Baril-Wileman Member 83%. **G** Alevo 94%. **H** Fairholme 'C' 99%.

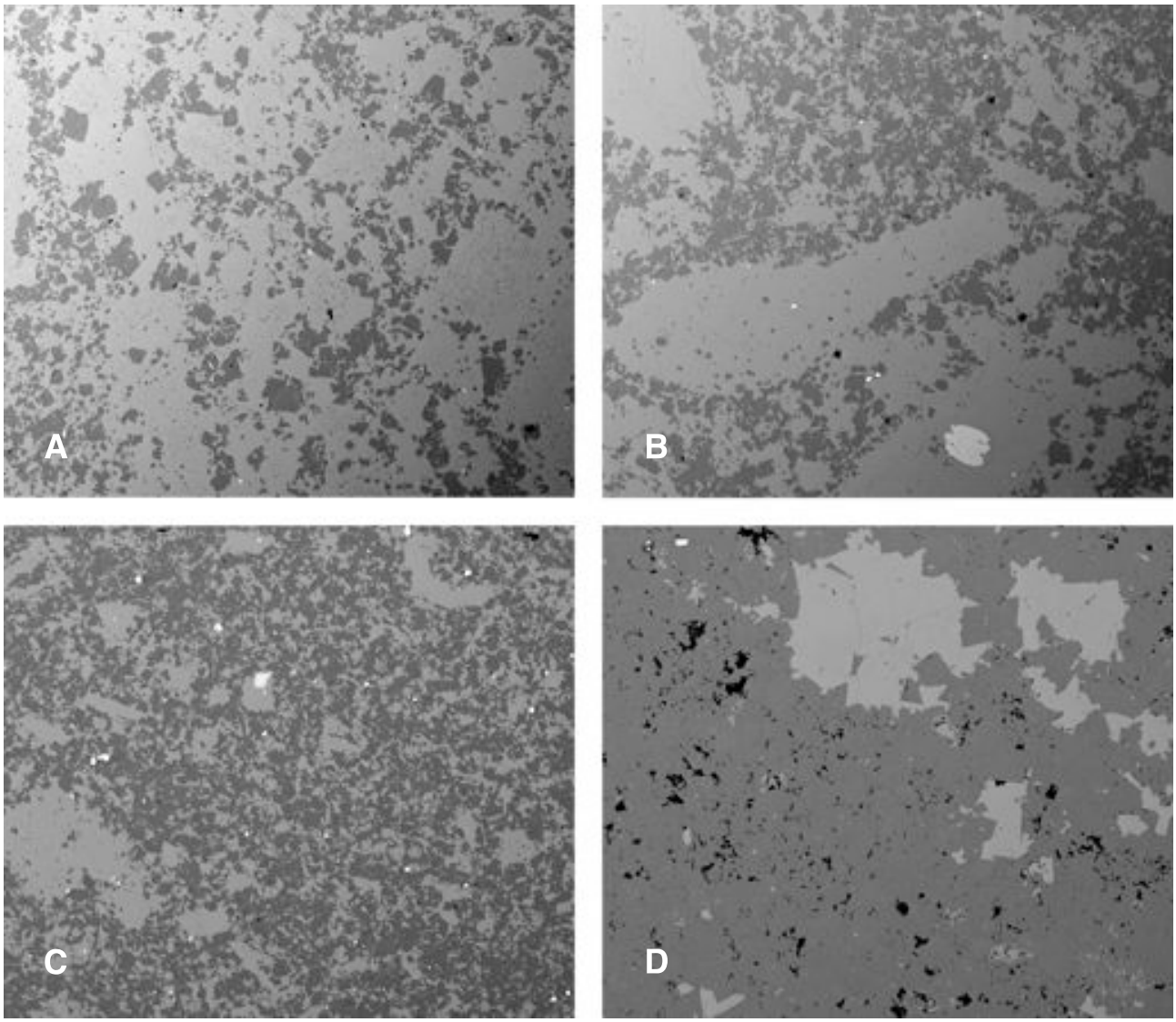

Figure 3: Protoliths from SEM backscatter imaging showing dolomite-calcite distributions. The dark grey is the dolomite, the light grey the calcite, and black spots are porosity. White mineral grains are accessories such as quartz and pyrite. All fields of view are $1.8mm$ across. **A** Salter 31%. **B** Loomis Member 34%. **C** Loomis Member 43%. **D** Baril-Wileman Member 83%.

3.1.4 Loomis Member – 43% Dolomite

This Loomis Member sample provides a dark grey stylolitic dolomitic limestone rock closest to the middle of the range of dolomite content. Pycnometry measurements indicate an average porosity among sample cores of 0.3%. Thin section characterization (Figure 1 D) shows an approximate 35% micrite and 65% visible dolomite and calcite grain composition. The dolomite is very fine grained, representing the smaller size end of the grain distribution, and the calcite grains are similarly small with rare millimeter scale grains interspersed. Larger calcite grains have irregular grain boundaries and length to width ratios. From SEM backscatter images the dolomite is well distributed and able to connect for lengthy pathways of support among grains (Figure 3 C). Calcite is twinned (spaced at the scale of 5 to 30μm) and stylolite solution seams are present. The stylolites have an average peak-to-peak amplitude of 2.6mm, an approximate periodicity of 5mm, and a thickness between 10μm and 500μm. They are composed of dark, fine oxide or carboniferous material. Two subhorizontal stylolite seams are present in the core. Common vertical seams filled with similar material connect the two stylolites (Figure 1 D). The stylolites are considered to be a common natural phenomenon that would provide a natural error source that could be accounted for in both post-deformation textural analysis and comparison to other rocks in the suite, namely the Salter Member 31% dolomite, and the Loomis Member 34% dolomite.

3.1.5 Opal Member – 48% Dolomite

The Opal Member sampled is a black limestone composite rock, consistently without visible grains at hand sample scale, resulting in the small average grain size and its standard deviation (Table 5) from thin section measurements (Figure 2 E). The XRF data shows a high silica content of 14% (from Table 4) which adds a dimension to the deformation system undesired in this experimentation. Samples were experimented on and results are briefly reported on in this writing, but extensive analysis was not performed as its characteristics do not to pertain to the purpose

of this experimentation.

3.1.6 Baril-Wileman Member – 83% Dolomite

The Baril-Wileman Member sampled is a creamy brown-grey coloured dolomitic limestone with visible millimeter-sized calcite grains at hand sample scale. Pycnometry measurements indicate an average porosity among sample cores of 3.4%, a value much higher than sample types previously outlined in this section. This aspect did not exclude the Baril-Wileman Member from interpretation and analysis of the results; the Member was the only sample with nearly desirable characteristics between the Loomis Member 43% and the end member dolomite, Fairholme 'C' (outlined below). Thin section characterization (Figure 2 F) shows a small composition of micrite, approximately 10%. Medium sized equant, subhedral dolomite crystals make up the bulk of the matrix. Figure 3, shows an example of the dolomite-calcite distribution from SEM imaging. The porosity is fairly evenly distributed and appears slightly vuggy. Some dolomite grains show minor internal cracks along cleavage orientations. The larger calcite grains are twinned in two opposing cleavage orientations, spaced on a $20\mu m$ scale.

3.1.7 Alevo Formation – 94% Dolomite

The Alevo Formation samples are creamy brown porous dolomitic limestones. The porosity is visible in hand sample, looking very well distributed in thin-section (Figure 2 G) and pycnometry measurements indicate an average porosity among cores of 6.3% with a high standard deviation relative to other rock types measured. Samples were experimented on and results are briefly reported on in this writing, but extensive analysis was not performed as its high porosity did not pertain to the purpose of this experimentation.

3.1.8 Fairholme 'C' – 99% Dolomite

The Fairholme 'C' Formation sampled provides the near pure dolomite end-member. In hand sample it appears as a light creamy brown-grey stylolitic rock with a very rough texture to the white weathered surface. Pycnometry measurements indicate an average porosity among sample cores of 1.6%, a slightly high value for the standard of the experimental suite, but within the tolerance. Thin section characterization (Figure 2 H) shows a larger grain size distribution than desired (Table 5) but is within reasonable natural expectations. Dolomite grains are equant, subhedral to anhedral with sharp angular grain boundaries. The stylolites present are characterized by angular lines of dark, fine oxide or carboniferous material (also Figure 2 H). They have an average peak-to-peak amplitude of $1.8mm$, an approximate periodicity of $2mm$, and a fine thickness on the micrometer scale. There is one stylolite solution seam in each sample deformed with the foliation plane perpendicular to the long axis of the core.

3.2 Experimentation

The mechanical behaviour and brittle constitutive laws of natural limestone and dolomite composite rocks sampled from the stratigraphy of the Rundle Group were determined in this research. All samples are sedimentary carbonates with no history of metamorphism. Cores measuring 30mm at the diameter were drilled and prepared for deformation in the Large Sample Rig (LSR) triaxial rock press (Figure 4) at the Center for Experimental Studies of the Lithosphere (CESL) established at the Department of Earth and Ocean Sciences, University of British Columbia (UBC) in Canada. An experimental grid was prepared for experimentation at three confining pressures, 25, 50 and 75 MPa, and for each rock type, differentiated by dolomite content.

3.3 Apparatus

The apparatus used, the LSR (Figure 4), is a triaxial rock press that uses an Argon gas confining pressure system, capable of applying 100 MPa of confining pressure. It employs an electric motor driven gear assembly to provide a differential load at a maximum of 200 000 pounds. The load is transmitted through the gears to a thrust bearing that drives a saginaw ball bearing screw which raises the confining vessel into contact with the upper plate at a fixed displacement rate. Load data is collected through an external load cell between the pressure vessel and the upper plate and transmitted to the computer and is interpreted by the instrument management program Labview. Displacement is measured through an external displacement transducer and data is transmitted to the computer. Confining pressure can be measured from an analog gauge, but a pressure transducer transmits electronic data to the computer. A half-bridge strain gauge circuit for each gauge runs through a labjack, through the e-piston, and is completed by the strain gauges during experimentation, which are essentially 120 Ω resistors. Deformation of the sample deforms the gauges and the change in resistance is monitored through the change in voltage of the circuit. This change is interpreted by Labview and expressed as strain. All data collection can

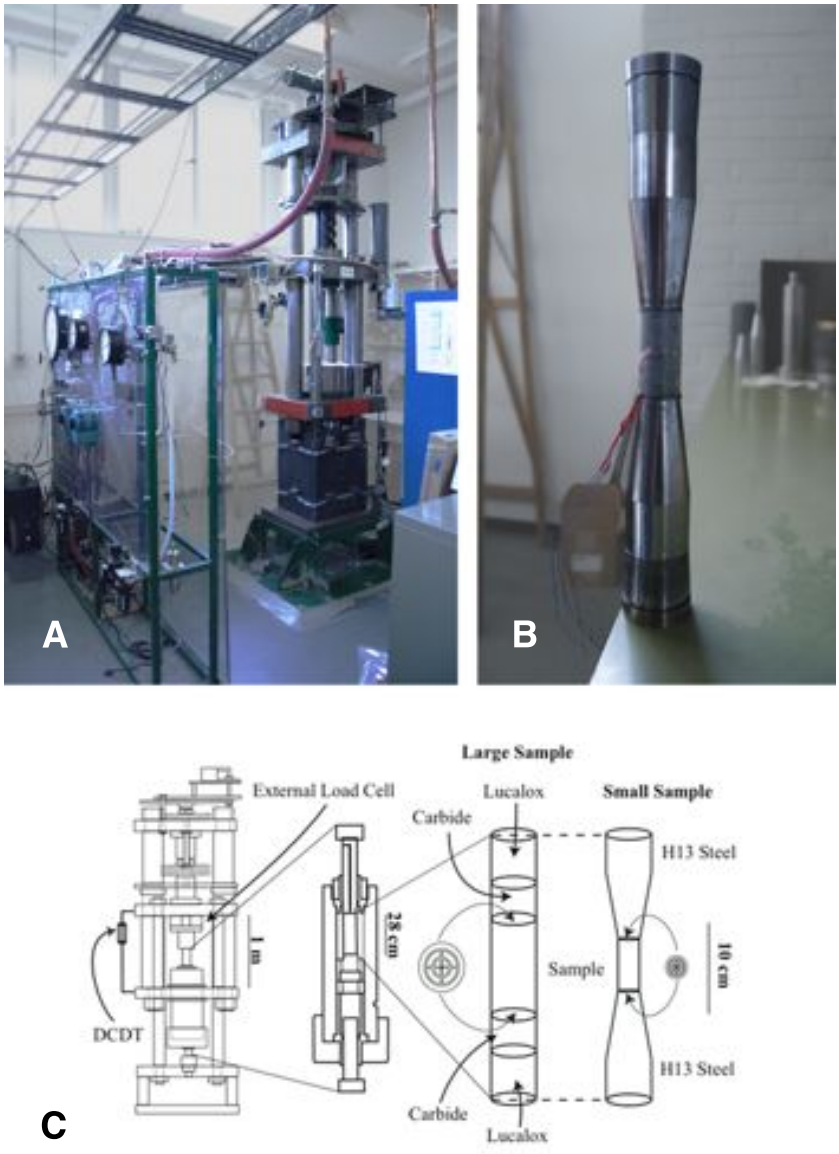

Figure 4: **A** The Large Sample Rig in CESL, UBC. **B** The sample assembly, without the polyolefin jacketing. **C** Schematic diagram of the rig. Taken from Austin [1].

be monitored in Labview during experimentation. The rate of collection of data is approximately one datum per 0.6 seconds.

3.4 Sample Preparation

All samples were inspected for foliation and if present cores were drilled perpendicular to the foliation surface. The cores, of diameter 30mm, were cut at each end to a length of 60mm and machined right, flat and parallel to within one thousandth of an inch tolerance. The core samples were cleaned of grit and dust in a sonic bath for ten minutes and then desiccated in an oven at 90 degrees celsius for twenty-four hours. When cool, the core samples were accurately weighed three times and their diameter and length were each measured six times in each axis orientation on the sample (Table 1). A helium pycnometer was used to accurately measure the bulk volume five times (measurements found in Table 1). From the averages of these measurements both the porosity and density of each sample was calculated. One sample of each rock type was sent to ALS Chemex Vancouver for x-ray fluorescence (XRF) oxide analysis (details in the Appendix). The comparison of density data (from Table 3) and percent dolomite content calculated from the XRF data (found in Table 4) is shown in Figure 5.

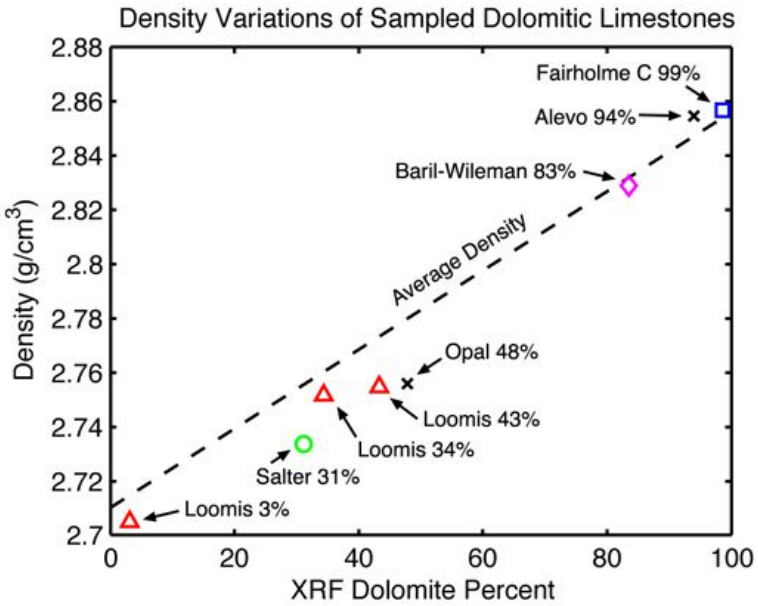

Figure 5: Average density of samples versus dolomite percentages calculated from XRF analyses.

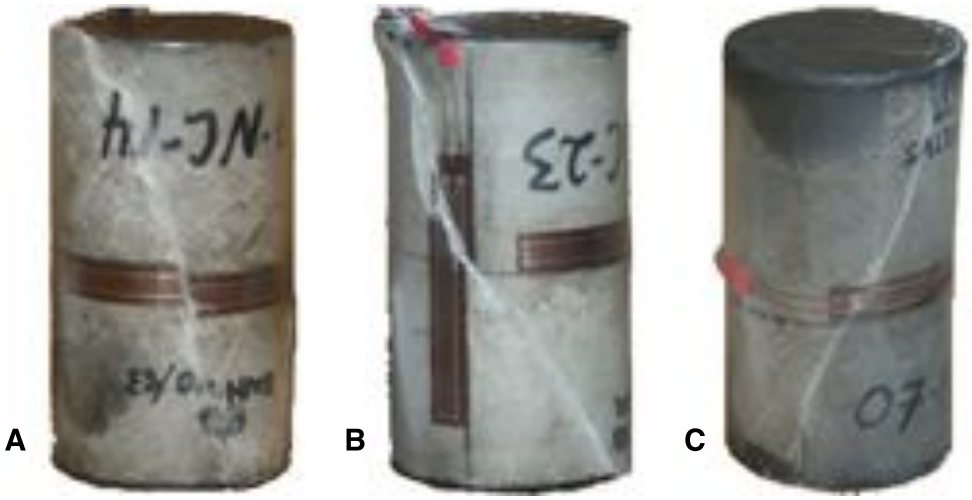

Figure 6: Deformed cores – **A** Baril-Wileman member at $P_c = 25$ MPa. **B** Fairholme 'C' at $P_c = 50$ MPa. **C** Salter Member at $P_c = 75$ MPa.

3.5 Strain Gauges

Strain gauges were affixed to the samples with a cyanoacrylate adhesive to collect data for analysis of Poisson's Ratio during deformation. One strain gauge was attached to each sample to record the vertical axial strain (parallel to σ_1), while another was attached perpendicular to record the horizontal strain due to the vertical compression, or the transverse strain (see Figure 6). Poisson's ratio (ν) gauges the response of transverse strain to axial strain: $\nu = -\frac{\varepsilon_{trans}}{\varepsilon_{axial}}$

3.6 Sample Assembly Preparation

Each sample is prepared for insertion into the pressure vessel by securing it between appropriately sized spacers and then between the upper and lower piston cups, using polyolefin shrink wrap to hold the entire assembly together (see Figure 4). The upper and lower ends of the polyolefin jacket are wired shut to block entry of the confining medium. The polyolefin jacketing prevents the Argon gas confining medium from infiltrating the sample. Argon gas is known to permeate through the polyolefin jacketing, but during the time-scale of these experiments the amount transmitted through is negligible. Fine gauge leads were run through small holes pricked in the polyolefin shrink-wrap jacketing used to isolate the sample from the argon gas. The holes are sealed with cyanoacrylate adhesive, a small pad of silly-putty, and five minute epoxy to prevent argon gas leaking in over the time-scale of the experiment. The leads are attached to the circuit in the lower piston outfitted for the electronics.

3.7 Data Reduction

As there is plenty of extraneous data collected for each experiment (see Figure 7) a data reduction process is performed on each data set to isolate the portion that is pertinent to the results. A Matlab program was written for the task and it extracted the relevant information of differential load, the associated displacement, and converted such input signals into useful values, respectively

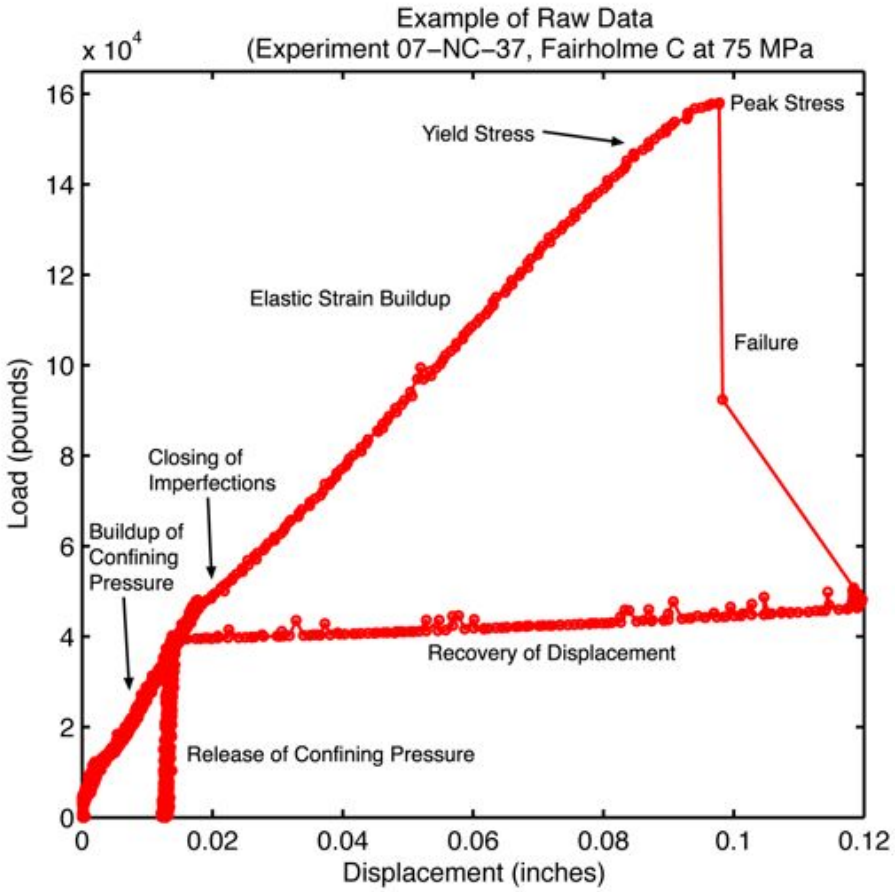

Figure 7: Example of an entire raw data set. The set is the same experiment used for example previously in Figure 8, Fairholme 'C' at $P_c = 75$ MPa.

differential stress and strain. Stress versus strain curves were generated and values for peak strength, yield strength, and maximum strain were isolated to establish results for judgement of failure criteria. The complete process for reduction and calculation of reported values is found in the Appendix (see page 64).

4 Mechanical Results

Forty-three rock cores of eight different dolomite compositions were deformed at a constant displacement rate of $1.8^{-2} cm\ s^{-1}$ under various confining pressures in the LSR. Mechanical loading was stopped immediately after failure of the sample denoted by a sudden drop in the load reading (Figure 7) and an accompanying, often loud, acoustic emission caused by the rapid release of stored elastic strain energy in the sample. Cores have visible deformation as either a single planar fracture plane or a network of distributed cracks, commonly in synthetic orientations (Figure 6). Table 2 shows the averages angle between the main failure surface and the σ_1 orientation by confining pressure and by dolomite percent.

4.1 Stress – Strain Relationships

Analysis of stress versus strain plots allows interpretation of the rock's response to the induced stress at the selected strain rate (Figure 8).

The stress versus strain curves, at each dolomite percent, are displayed in Figure 9 segregated by confining pressure. They show peak strengths ranging from 307 to 703 MPa, from the least confined Loomis Member 3%, at P_c = 25 MPa, to the most confined Fairholme 'C' 99%, at P_c = 75 MPa, respectively (see Table 2). In general samples with a higher dolomite content were stronger than calcite rich rocks. The mechanical strength appears to increase fairly linearly with increasing confining pressures, within the experimental testing range, for most dolomite compositions (Figure 10). The Salter Member 31% proved strong relative to the Loomis Member 34% at the lowest confining pressure. The strength of the Loomis Member 34% benefited more from confining pressure and proved substantially stronger than the Salter Member 31% in the P_c = 50 and 75 MPa experiments. The Loomis Member 43%, noted with its stylolite solution seams and vertical connecting structures consistently, failed at strengths below that of Loomis 34%. The Opal Member 48% was remarkably strong, and with its fine grain size and silica

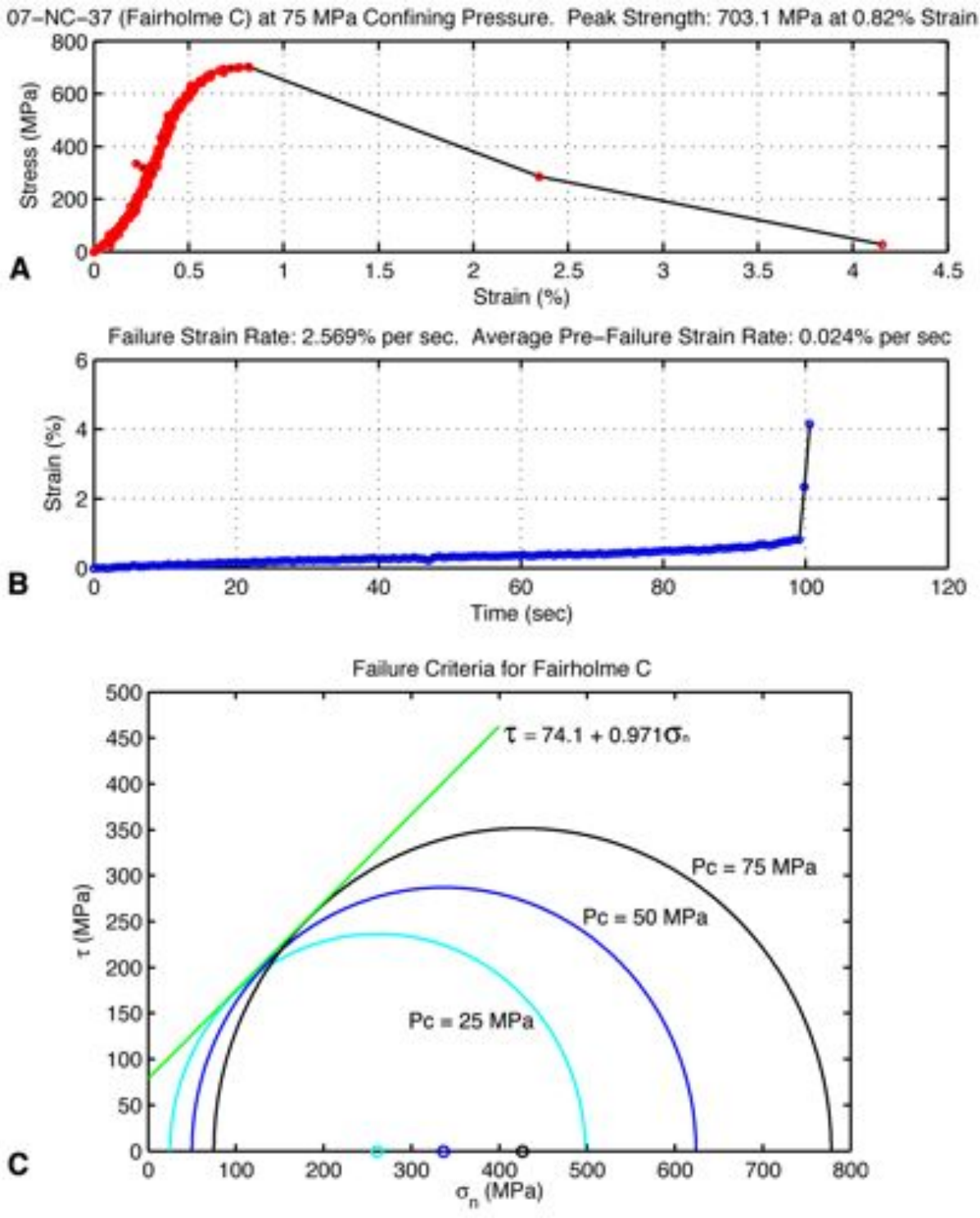

Figure 8: **A** Stress – Strain curve for Fairholme 'C' at $P_c = 75$ MPa. **B** Strain versus Time to gauge changes in strain rate. **C** Mohr diagram with Coulomb failure criterion for the Fairholme 'C' series.

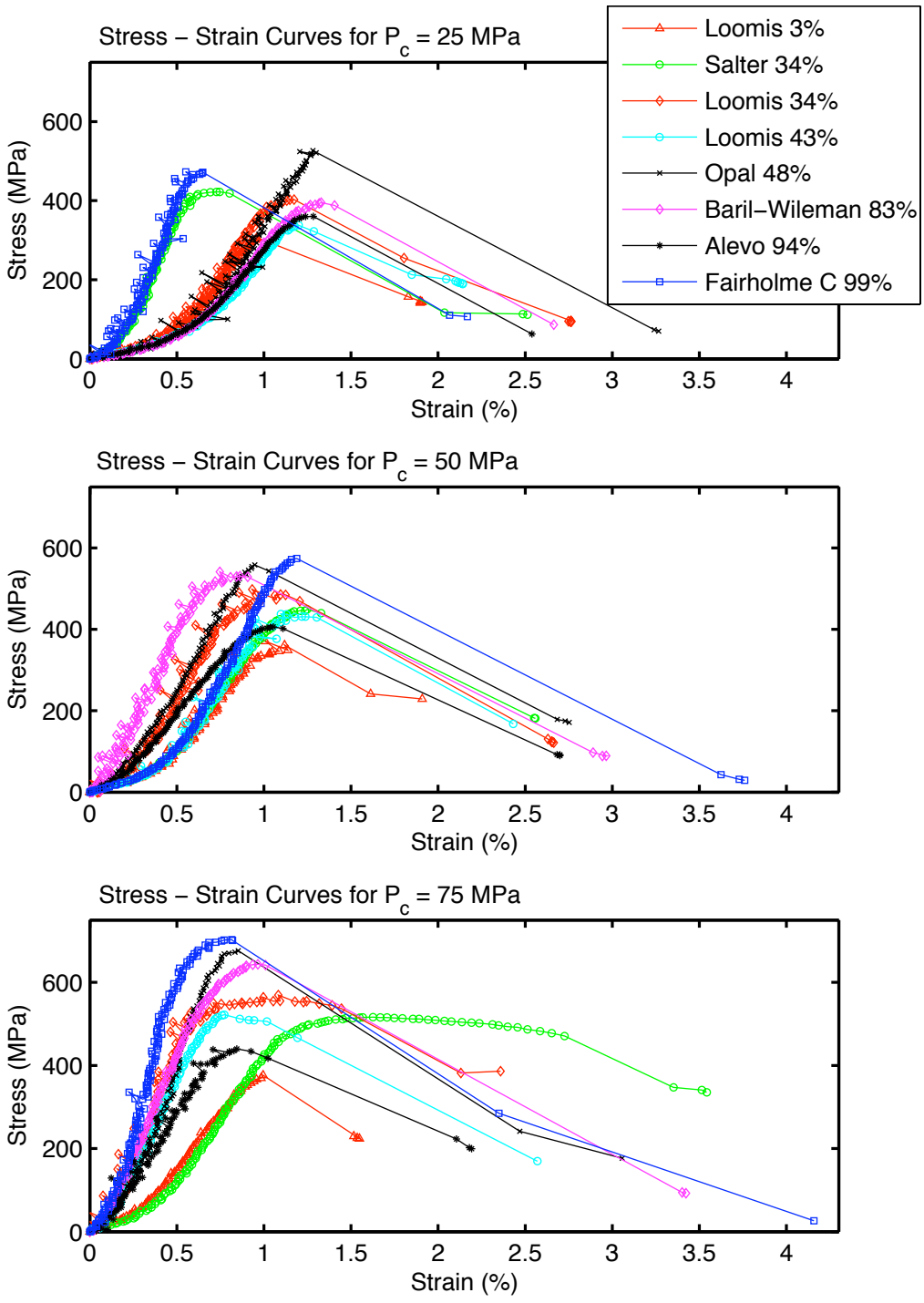

Figure 9: Cumulative stress–strain curves separated by confining pressures ($P_c = 25$ MPa at top, $P_c = 75$ MPa at bottom).

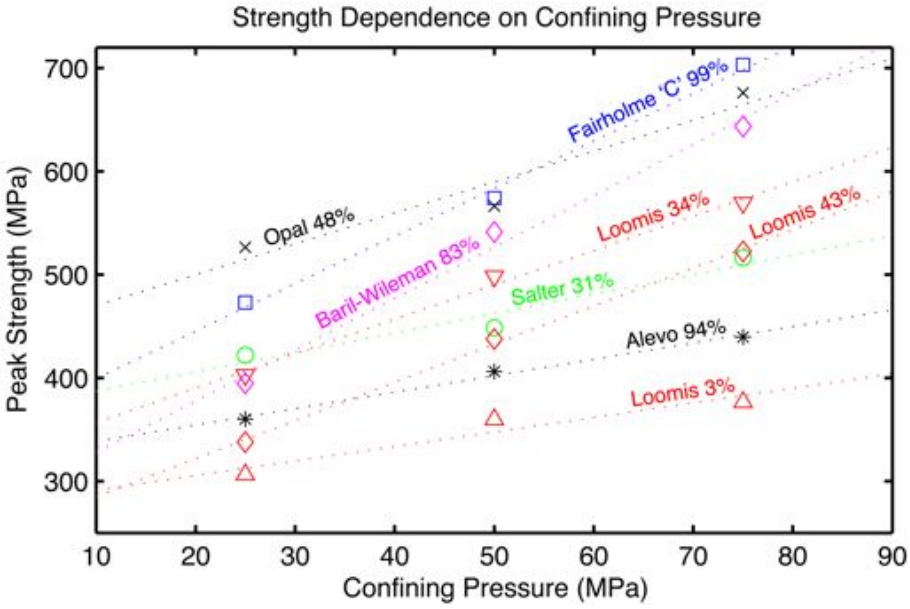

Figure 10: Strength dependence on confining pressure for each dolomite composition.

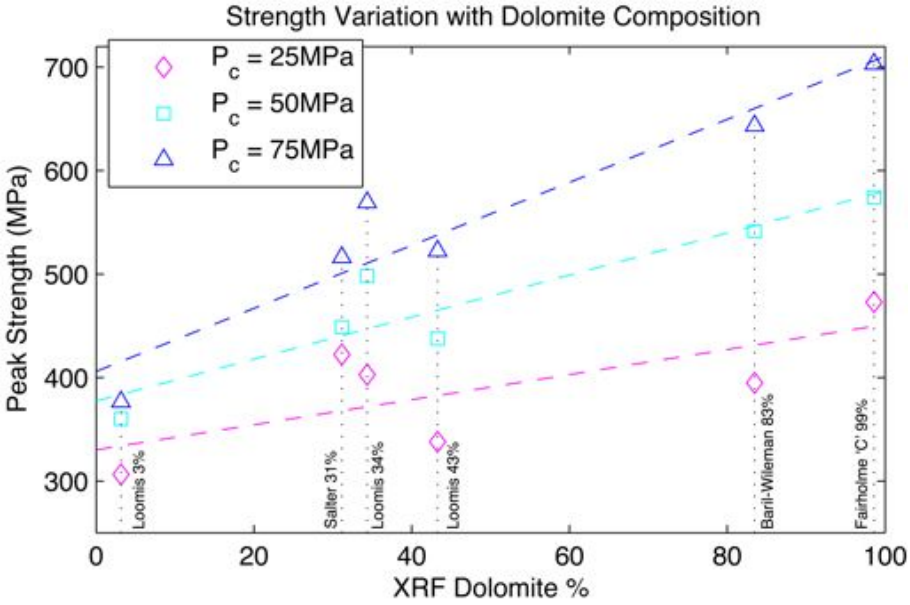

Figure 11: Strength variation with dolomite composition at each confining pressure. The dashed lines are linear fits to the data.

content was considered less appropriate for inclusion in the suite. The Alevo 94%, noted for its high porosity, produced consistently weak results.

There is a mixture of styles of response seen in the stress–strain curves. There are various scales of initial response whereby the pore space and imperfections are closed. Some samples responded with linear elastic strain quickly, whereas others took up to 0.6% strain before responding elastically. Each rock type had samples that responded in both ways, but generally, at the lowest confining pressure more strain was accommodated closing imperfections than at the highest confining pressure. Overall, the Young's Modulus, (calculated with linear fits to the elastic portion of each stress-strain curve, Table 2), was highest at the highest confining pressures, showing the heightened capacity for the rocks to deform and store elastic energy before failure. The values for Young's Modulus at the lower two confining pressures showed few correlations with the confining pressure. Most rock samples yielded in a ductile fashion to, at least, a small degree before failure. At $P_c = 75$ MPa the Salter Member 31% yielded considerably before failure. Generally, the yielding effect was more pronounced at higher confining pressures and by high calcite content.

Excluding the Alevo Formation and the Opal Member due to their anomalous characteristics and behaviour, Figure 12 (with arrows denoting failure to allow for wider axis scaling) displays the data set used for all further analysis. Figure 11, shows the peak strength data for the select dolomite compositions at each of the three confining pressures. Linear fits to each data set at differing confining pressures provide the most simple perspective of the rate of increase of mechanical strength per percent increase in Dolomite at each P_c.

4.2 Mohr Diagrams

Limited development and dilation of Mode I (i.e. parallel to σ_1) fractures under a differential stress exploits the stress concentrations around inherent porosity and existing micro-fracture tips. Coalescence of Mode I cracks results in planar shear ruptures at thirty degrees from the differential stress, the plane where the ratio of shear stress component to normal stress component is highest.

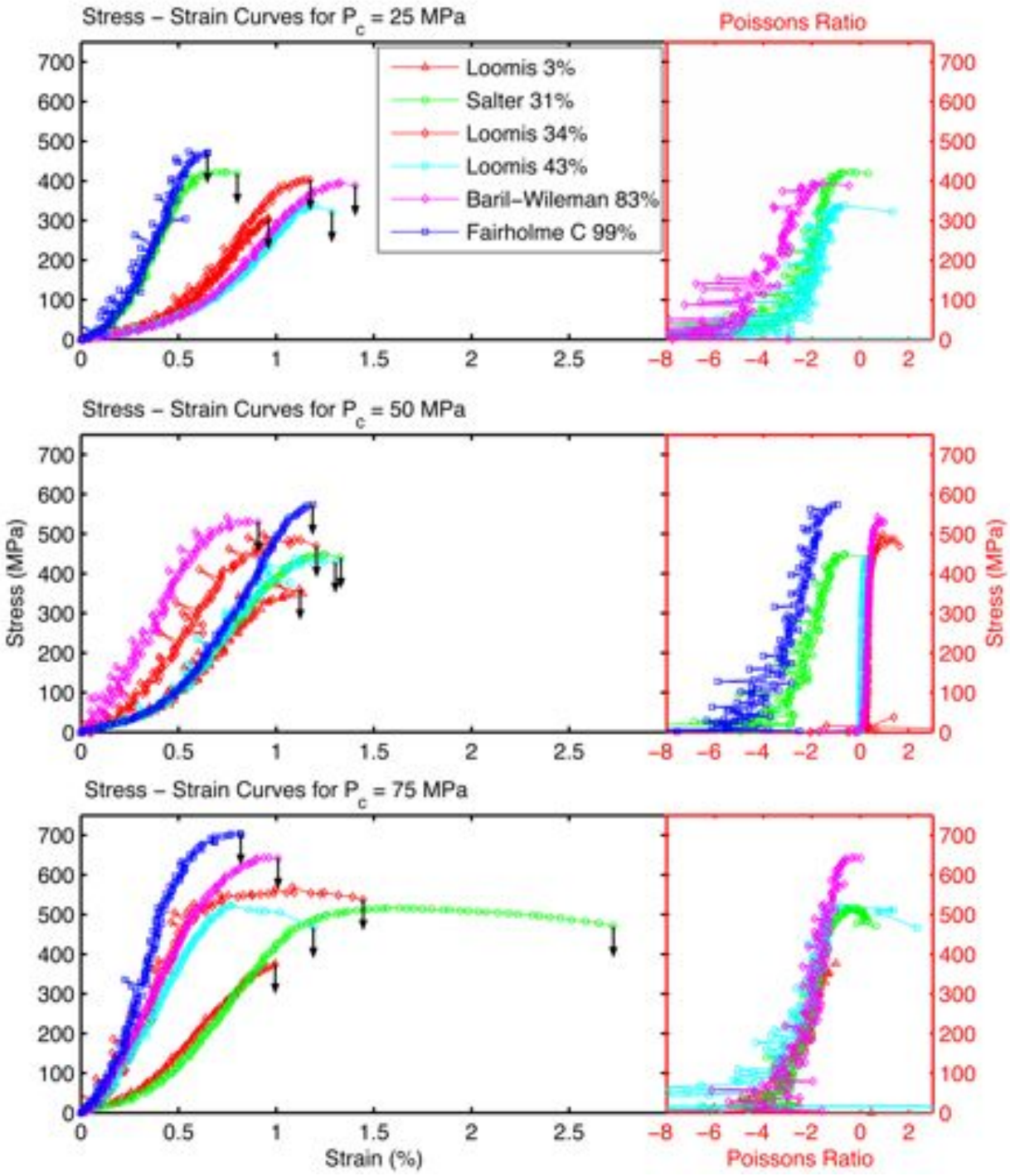

Figure 12: Cumulative stress–strain curves for dolomite compositions selected for textural analysis, with Poisson's Ratio evolution with stress at right.

Mohr diagrams parametrically relate the mean stress and the differential stress to the shear stresses (τ) and normal stresses (σ_n) acting on planes at all angles possible inside the deformed rock:

$$\tau = \frac{1}{2}(\sigma_1 - \sigma_3)\sin 2\theta$$

$$\sigma_n = \frac{1}{2}(\sigma_1 + \sigma_3) + \frac{1}{2}(\sigma_1 - \sigma_3)\cos 2\theta$$

Mohr-Coulomb failure criteria is developed from peak strength data of multiple experiments performed at varying confining pressures. The straight line defined by the internal cohesion (C) and the coefficient of internal friction (μ) expressed by the shear stress as a function of normal stress:

$$\tau = C + \mu \times \sigma_n$$

gives a criteria for which a given stress state can either be stable or in excess of the conditions needed for shear failure. Figure 8 provides an example of a single Mohr diagram using the Fairholme 'C' series. From the experiments run at three confining pressures Mohr diagrams were constructed from the measured peak strength. Figure 13, is a collection of all the Mohr diagrams made for all the peak stresses attained at all three confining pressures and all eight dolomite compositions. The calculated failure criteria are listed in Table 6. The Mohr-Coulomb failure criteria developed for each were plotted to the $\sigma_n = 350$ MPa point and linear interpolations were made between each criterion to create a failure surface for the sample suite. The cohesion varies slightly throughout the dolomite scale, low values roughly correlating to the expected sources of flaws – namely porosity (eg. BW 83% and Fairholme 'C' 99%) and existing structural weakness (eg. Loomis 43%). The cohesion of the Salter Member 31% was dramatically higher being a clean and tight fine grained rock. The coefficient of internal friction fairly consistently increases with increasing dolomite percent signifying that dolomite is an important parameter in the strength of dolomitized limestone rocks.

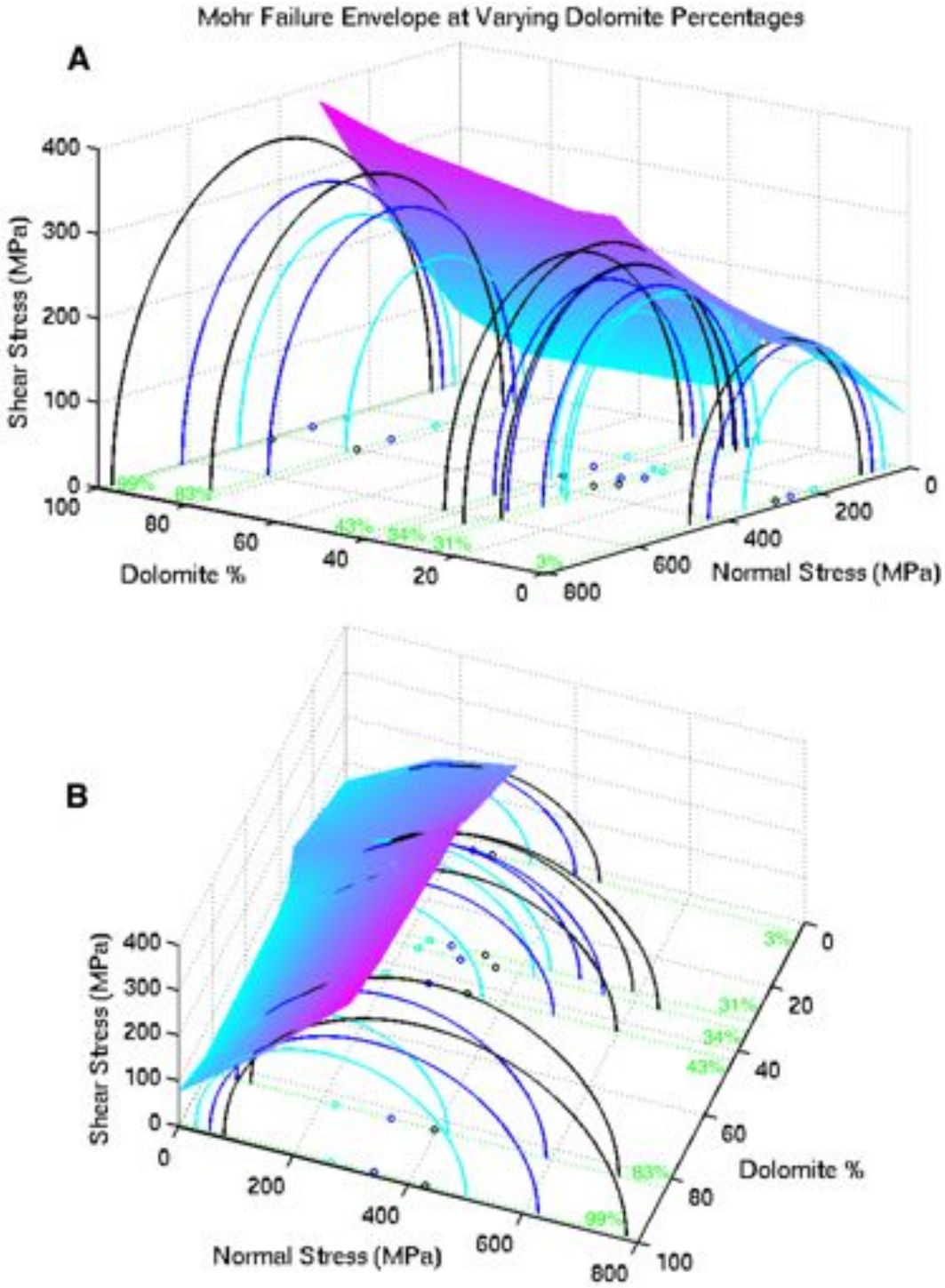

Figure 13: Mohr-Coulomb failure criteria at various dolomite compositions represented by the surface. The colouration of the surface has no meaning other than height along the vertical axis.

4.3 Strain Gauges and Poisson's Ratio

The strain gauge results were slightly enigmatic. There were two types of responses produced, with little to no correlation towards any specific cause or feature inherent in the sample suite. The two types of responses can be expressed as an evolution of Poisson's ratio during loading (see Figure 14). One response is entirely negative, meaning that there was a volume reduction during deformation, the other response entirely positive, meaning that the transverse dimension expanded during axial contraction from loading. The scale of the strain responses for each was different; the scale of strain for the gauges in the negative Poisson's ratio response was generally around 0.5, and the scale of strain for the gauges in the positive Poisson's ratio response was generally larger than 2 (sometimes much higher). The range of the strain calculated from the displacement transducer did not show differing scales for experiments of each type of Poisson's ratio response. This issue was not resolved as no correlation from response to any characteristic was found, but the information was self-consistent between the scales of the two gauges on each sample, so the ratio still seems relevant. The response of volume reduction, in theory linked to porosity collapse at the initiation of loading, yielded no correlation to measured porosities in this experimental run. Both tight rocks and porous rocks experienced both types of response at various confining pressures (see Figure 12). The only effect that could possibly be considered to show post-deformation during analysis of the deformation to differentiate the two responses would be the production of Mode I fractures prior to the creation of a through-going macroscopic failure surface. Samples that produced a volume reduction response theoretically should not show as developed Mode I fractures as a sample that produced a response with a positive Poisson's ratio, as the transverse expansion would permit enhanced dilation of fractures in a Mode I orientation. One possible macroscopic product of this effect would be that sample that underwent volume reduction during deformation would create overall less distributed strain, perhaps having only a single failure surface. The opposite response would then show more distributed strain. Observations supporting these theories will be noted

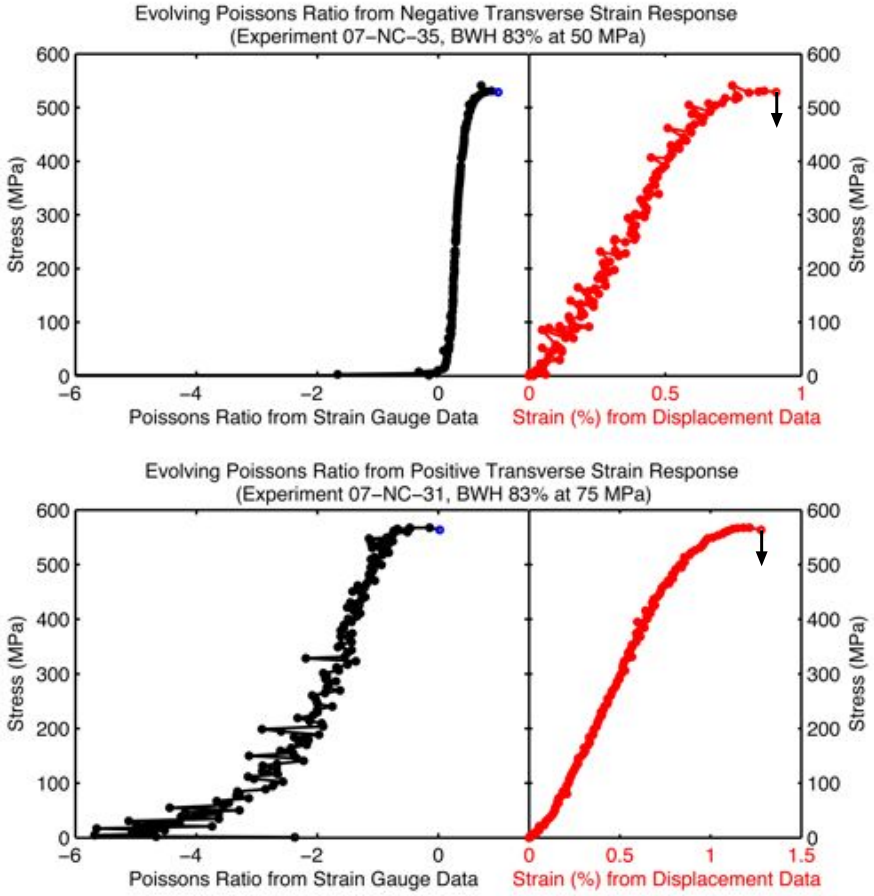

Figure 14: Two different responses of Poisson's Ratio with applied stress. The top plot is a result of a contracting vertical axis and expanding transverse axis. The bottom plot is a result of a contracting vertical axis and an initially contracting transverse axis that reverses half-way through the experiment and expands back to zero strain prior to failure.

during the following section of analysis of the post-deformation microstructures.

4.4 Repeated Experiments

After the experimental array had been accomplished the data was analyzed by calculating Mohr diagrams and failure criteria for each dolomite composition. The Mohr diagrams produced showed deficiencies in the data that proved confusing when attempting to establish failure criteria. Some peak strengths produced did not contribute to the criteria. A few of the $P_c = 75$ MPa experiments produced Mohr circles smaller than the $P_c = 50$ MPa circles. In these cases the peak strength data showed a decrease from the moderate confining pressure to the high confining pressure. Further analysis of this problem discovered that the mean stress was still higher in the higher confining pressure experiments even though the maximum differential stress reached was lower than in the medium confining pressure ones. These experiments were reproduced and, eventually, the peak strength data reported on in this paper were yielded. Six $P_c = 75$ MPa experiments were repeated, three $P_c = 50$ MPa experiments were repeated, and one $P_c = 25$ MPa experiments was repeated. The reason for numerous experiments to be done at higher confining pressures to produce accurate data that represents the lithologic strength capacity of the rock is due to the imperfect nature of the samples. Higher confining pressures create the situation where larger amounts of ductile strain may occur before failure giving the highest chance to exploit compromising natural defects and imperfections in the sample. The peak strengths reported are the largest of all data from experiments performed at their respective dolomite composition and confining pressure. It also must be noted that judgement on behalf of the experimentalist was used to choose which experiments to reproduce. The Mohr diagrams eased the notice of undesirable high confining pressure peak strength data. A smaller percent-difference in the data produced obviously limiting results than differences in lower confining pressure data.

4.5 Grain Size Distributions

Grain size was measured using a 'line-length' technique whereby one hundred 'average' diameter grain sizes were measured. Some larger grains had high aspect ratios, up to 3:1. The presence of larger grains in a fine matrix means a bimodal distribution. The method used was not considered an accurate statistical measurement for quantitative analysis merely a tool for qualitative analysis. The calculated averages and standard deviations (Table 2) only represent a gauge of the norm and perhaps an indication of the bimodal distribution.

The dolomite grains are generally represented by the fine portions of the measured grain size distributions (micrite was not measured in this fashion). In higher dolomite content samples the calcite content was generally restricted to the larger grains in the distribution.

5 Textural and Microstructural Analysis

Although dolomite content is the most important parameter, dolomite replacement textures, the influence of internal structure and the dolomite spatial distribution are also deterministic parameters with regard to the strength of dolomite–limestone composites. It is understood that the mechanical responses and data are limited in their general application to dolomite – limestone composite rocks similar in texture to the sampled rocks.

5.1 Deformation of the Loomis Member 3%

The Loomis Member 3% is a very weak rock as expected since it has a low dolomite content. Diffuse, irregular grain boundaries and micritic matrix eased the propagation of transgranular fractures. The strengthening effect of confining pressure seems limited, as ductile yielding onsets at a low stress at higher confining pressures. Samples exhibited some of the most common mechanisms of failure initiation and strain distribution. Strain localized into fine comminution zones lining the wall of the main ruptures. Blocks of wallrock lie in various states of disaggregation inside the damage zone (Figure 15). Intergranular cracks occur down to the scale of the micrite grain boundaries towards the edge of the damage zone. Comminuted and pulverized fragments have various shapes from irregular and angular to cleaved to rounded. Disaggregation from bent and fractured sections between cleaved twin planes is common throughout.

The matrix showed a tendency to disaggregate along grain boundaries distributed away from subsidiary fractures (Figure 16 D, bottom-right of image) easing redirection of propagating fractures into favorable orientations (Figure 16 B).

Twin planes in large calcite grains interspersed throughout the rock provide weak cleavage planes exploited by fractures propagating at various times during loading (Figures 15 and 16). Shear fractures propagate parallel to twin planes creating minor amounts of comminuted material directly in the rupture zone. This usage of cleavage was very common at all confining pressures.

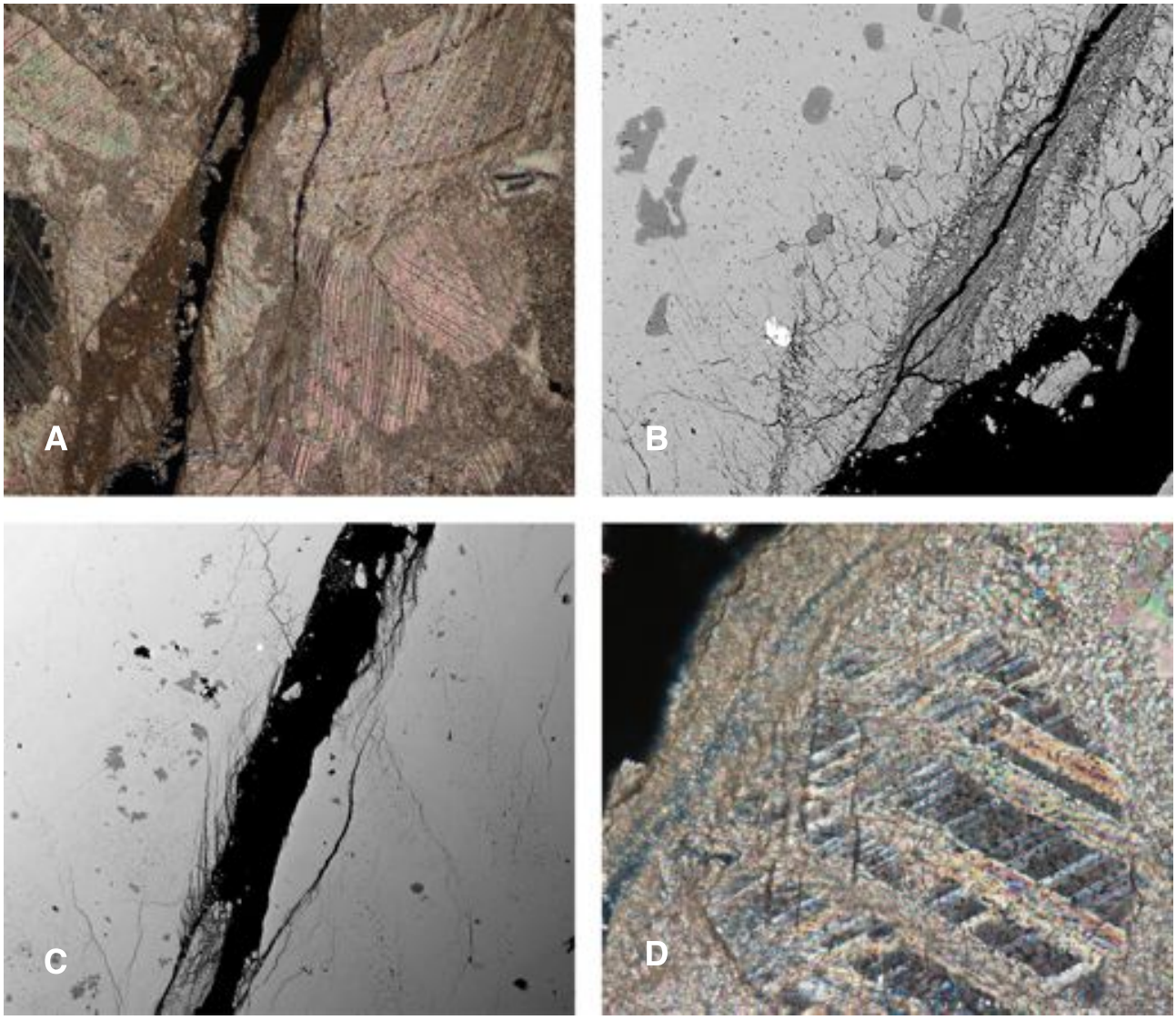

Figure 15: Comminution and offset Mode I fractures in Loomis Member 3%. *In each SEM backscatter image the dark grey matter is dolomite, the light grey is calcite and black represents voids from fracture or porosity.* **A** *Optical micrograph (XPL). Width of view* = $1.5mm$. The lower left wall rock is heavily comminuted. Subsidiary fractures in the upper right wallrock exploit weak twin planes in calcite crystals **B** *SEM backscatter image. Width of view* = $330\mu m$.Vertical cracks along twins in calcite has been bent from displacement. The subsidiary fracture caused disaggregation and comminution of the bent and cracked twins. **C** *SEM backscatter image. Width of view* = $1.5mm$. Large vertical fractures offset by displacement. **D** *Optical micrograph (XPL). Width of view* = $300\mu m$. Intragranular cracks prior to offset created fine scale twinning in the twin orientation oblique to the fracture orientation.

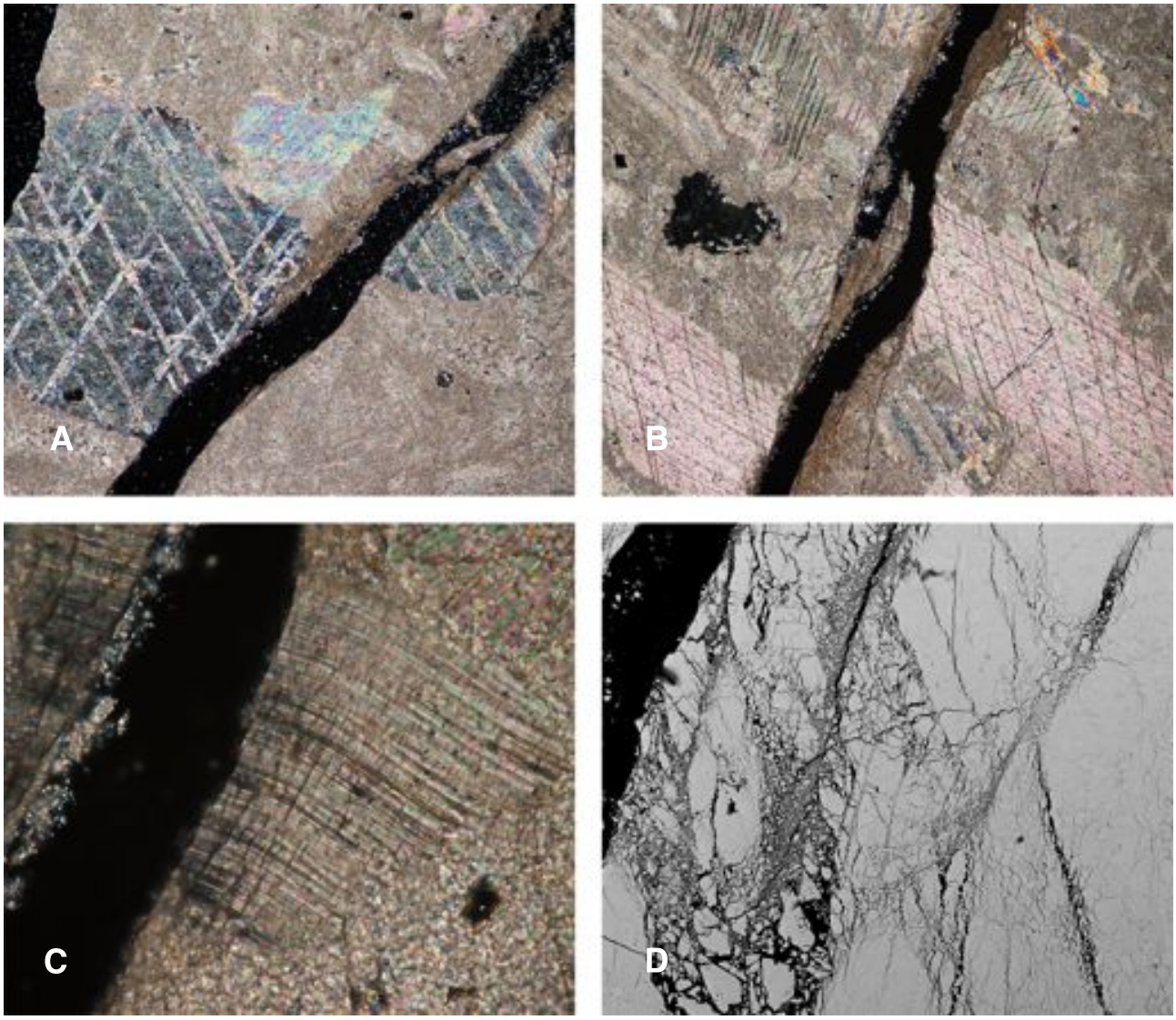

Figure 16: Cleavage exploitation and fracture propagation control factors in Loomis Member 3%. *In each SEM backscatter image the dark grey matter is dolomite, the light grey is calcite and black represents voids from fracture or porosity.* **A** *Optical micrograph (XPL). Width of view* $= 1.5mm$. Failure occurring parallel to twin planes, offsetting the grain. **B** *Optical micrograph (XPL). Width of view* $= 1.5mm$. Failure occurring oblique to twin orientations. Subsidiary fractures exploit the twins and cleavage in the offset large grain on the right. The fracture continues through micrite and orients parallel to twins in the top grain. **C** *Optical micrograph (XPL). Width of view* $= 300\mu m$. Fracture propagation perpendicular to twin orientation causes heavy damage within the grain. **D** *SEM backscatter image. Width of view* $= 450\mu m$. Subsidiary fractures exploit weak cleavage intersections.

Fractures ripping through grains perpendicular to existing twin planes show extensive internal damage (Figures 16 B and C). This feature was common only at higher confining pressures. Offset through failure often locally bent twinning (Figure 15 B) in larger calcite grains. Fine scale twinning was occasionally created during deformation in calcite grains close to damage zones (Figure 15 D) even developing to accommodate strain in an existing twin orientation oblique to vertical intragranular cracks that opened prior to failure. Subsidiary fracture paths favoured cleavage intersections (Figure 16 D).

The small amount of dolomite in the samples may have had only a small bearing on the mechanisms of failure in the Loomis Member 3%. The dolomite was finely disseminated and slightly concentrated in the larger calcite crystals, grading from larger to smaller from the centers outwards. They inconsistently show light concentrations of fractures around them implying their presence only affected deformation to a small degree. The only load bearing network was that of the calcite grains.

Extensive development of long vertical Mode I cracks that propagated to lengths over one-half millimeter offset by shear failure were noted, primarily at higher confining pressures (Figure 15 C) and favouring exploitable cleavage. The experimental sample that produced Figure 15 underwent a positive Poisson's Ratio response, consistent with allowing such strain localization to occur.

5.2 Deformation of Salter Member 31%

The Salter Member was too fine grained for effective interpretation of many structures using a petrographic microscope therefore the observations below are limited to SEM backscatter images.

Thin comminution zones lined large portions of the walls of the rupture zone. Dolomite grains within the damage zone were fractured and disaggregated but contiguous calcite grains commonly showed a much finer degree of comminution implying that more strain energy was distributed into the calcite (Figure 17 A). Comminuted calcite and micrite particles were commonly finer than the grain size of the original micrite content. Intergranular cracks amongst micrite were common

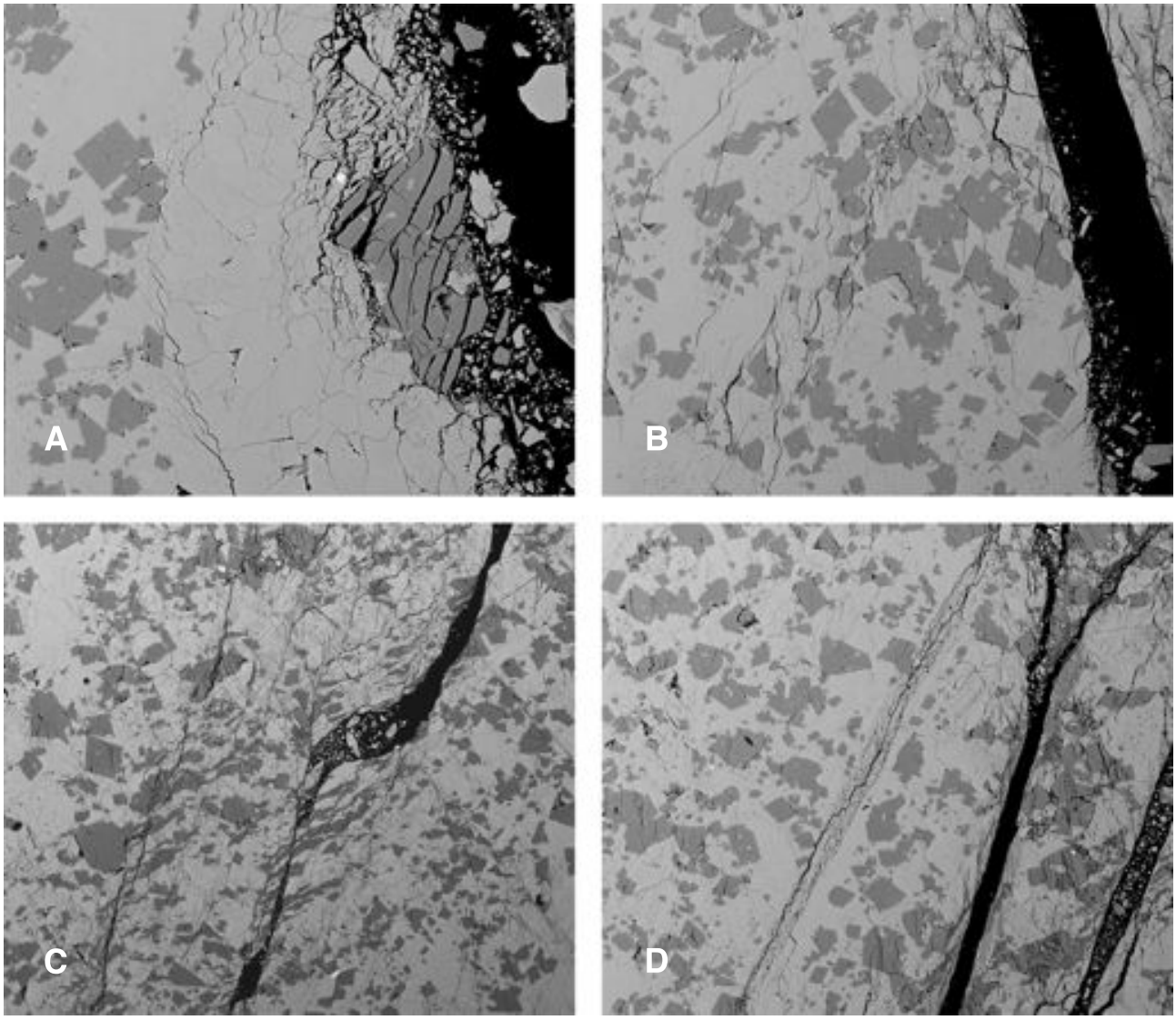

Figure 17: Deformation of Salter Member 31%. *All are SEM backscatter images. In each SEM backscatter image the dark grey matter is dolomite, the light grey is calcite and black represents voids from fracture or porosity.* **A** *Width of view* $= 370\mu m$. In the rupture damage zone dolomite breaks and disaggregates. The contiguous calcite above comminutes to a finer degree. The subsidiary fracture, left, avoids the dolomite content. **B** *Width of view* $= 670\mu m$. Distributed Mode I cracks isolated in the calcite content. **C** *Width of view* $= 900\mu m$. Shear bands in a high strain experiment that underwent considerable ductile yield. The compressional jog in the center would have been filled with gouge before vacuum impregnation with epoxy. **D** *Width of view* $= 770\mu m$. Circumstantially dolomite-free paths of calcite favour deformation while calcite is acting as the load-bearing phase.

through the extent of the damage zone (Figure 17 A).

Strain partitioning into calcite was very common in the Salter Member 31% as illustrated in Figure 17 A. Figure 17 B shows sub-vertical fractures in calcite beginning to coalesce in a shear rupture orientation. Figure 17 D has a fracture in the center that propagated in a linear fashion in a favorable shear orientation entirely through a band of calcite.

The spatial distribution of dolomite was fairly even but could not form long connective pathways of grain support. This prevented the effective use of dolomite's higher Young's Modulus to absorb more strain energy during deformation and this shows as a lack of cracking and comminuting of dolomite grains.

The Salter Member deformed at a confining pressure of 75 MPa underwent a ductile yielding to finally fail after sustaining 2.7% strain (data in Figure 12). This large amount of strain produced very distributed strain focused mainly amongst the calcite material. Deformation noted in dolomite grains were typically Mode I transgranular cracks. It also produced micro-scale shear bands in compressional jogs along the main fracture plane (Figure 17 C). The SEM image from Figure 17 C shows a black gap in the center signifying the main shear failure surface. This gap is assumed to have been originally filled with comminuted material, gouge, that was displaced during the vacuum impregnation process.

5.3 Deformation of the Loomis Member 34%

The textures of Loomis Member 34% differ from the Salter Member 31%. The Loomis is generally coarser grained with a wide size distribution that includes larger calcite grains. This textural change contrasts the styles of deformation. Fracture networks are distributed into large damage zones weaving throughout the rupture volume. The deformed Loomis Member 34% shows extensive comminution in the dolomite material implying a considerable partitioning of strain into it. With the presence of the larger calcite grains the dolomite is distributed in higher concentrations amongst the finer grains allowing for more dolomite grains to share common boundaries and

provide networks of support during differential loading. This contrast with the Salter Member is seen in SEM images where the main rupture paths have propagated through a series of closely spaced or connected dolomite grains (Figures 18 A and B). Calcite masses contiguous with comminuted dolomite grains typically show a finer degree of grain-size reduction than the dolomite. The reduced size of the calcite was difficult to distinguish from disaggregating micrite, yet the size distribution of the comminuted particles commonly includes much smaller size scales. Near the outer limits of the damage zone, intergranular cracks occur along what is interpreted to be the micrite grain boundaries.

Calcite grains, larger than the micrite grain size, fracture along twin planes and disaggregate readily. Dolomite grains uncommonly separate along cleavage. Disaggregation is typically limited to irregularly shaped, often Mode I, transgranular fractures. Failure surfaces anastomoze through sub-vertical and shear orientations in areas of dolomite concentration. In areas of calcite concentration, subsidiary Mode I fracture arrays form in shear rupture orientations yet did not coalesce into macroscopic failure surfaces (Figures 18 A and B).

Euhedral crystals of dolomite contained in the centers of larger calcite crystals commonly remained whole while fracture networks in the calcite concentrated around them (Figures 18 C and D).

5.4 Deformation of the Loomis Member 43%

The Loomis Member 43% shows a weak peak strength at lower confining pressures, possibly due to the vertical infilled cracks that connect the stylolites, or just the stylolites themselves. Higher confining pressures would theoretically help keep such vertical planes of weakness from opening and allowing the fracture tip to propagate.

The larger calcite crystals are highly comminuted (Figures 19 A and C). Calcite grains contiguous with dolomite grains show finer comminution and a more regular particle size distribution. Comminuted dolomite particles have irregular shapes and a large distribution of sizes. Micritic

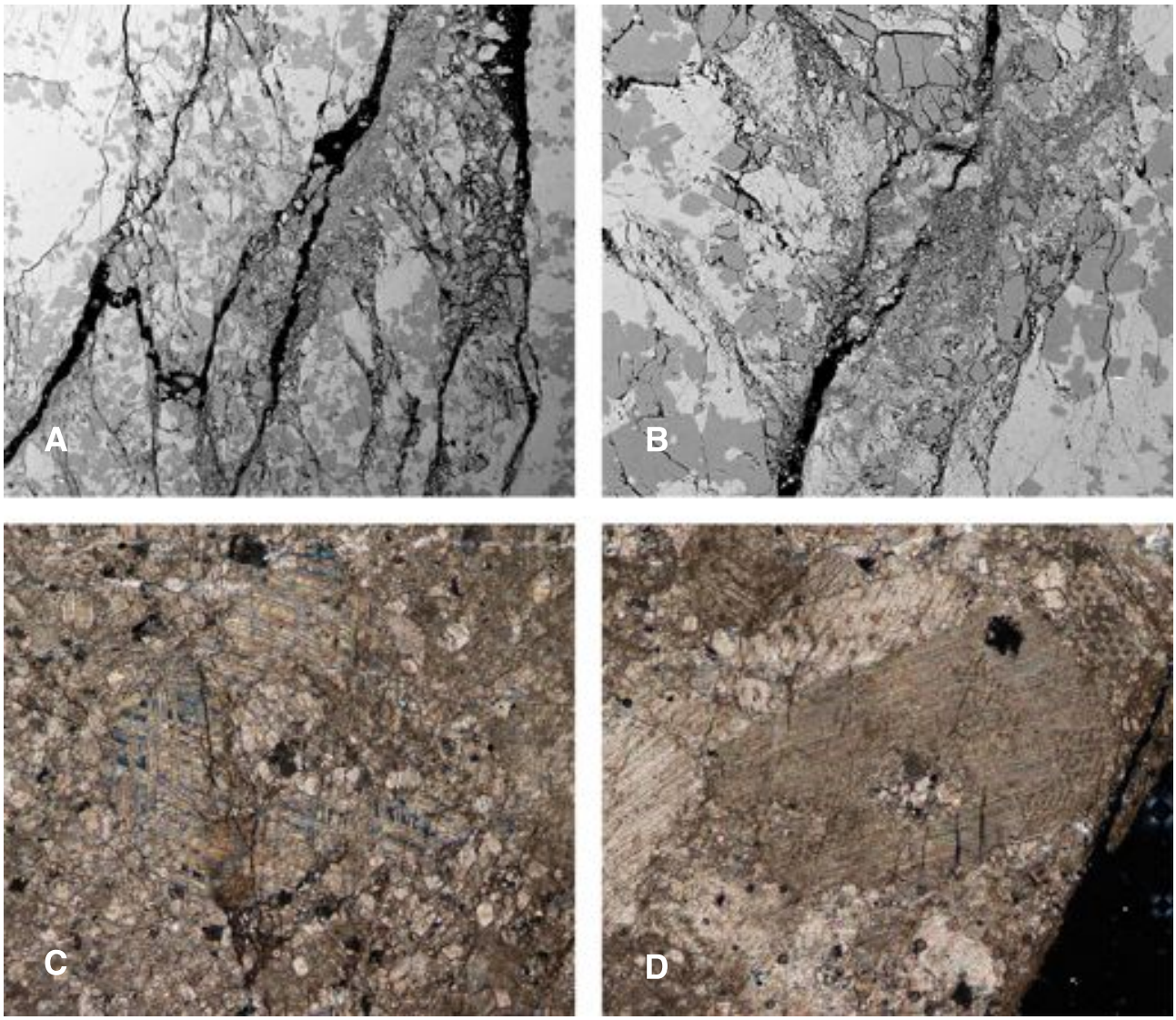

Figure 18: Deformation of the Loomis Member 34%. *In each SEM backscatter image the dark grey matter is dolomite, the light grey is calcite and black represents voids from fracture or porosity.* **A** *SEM backscatter image. Width of view* $= 1.5mm$. Larger calcite grains restrict the volume containing dolomite creating load-bearing support networks of dolomite grains. The stress released from these networks creates heavy cracking and comminution of the dolomite. **B** *SEM backscatter image. Width of view* $= 450\mu m$. Closeup of the comminution of dolomite. **C** *Optical micrograph (XPL). Width of view* $= 1.5mm$. Dolomite grains inside calcite grains enhance the deformation of the calcite grain. **D** *Optical micrograph (XPL). Width of view = 1.5mm.* Dolomite grains within a calcite grain promote transgranular cracking.

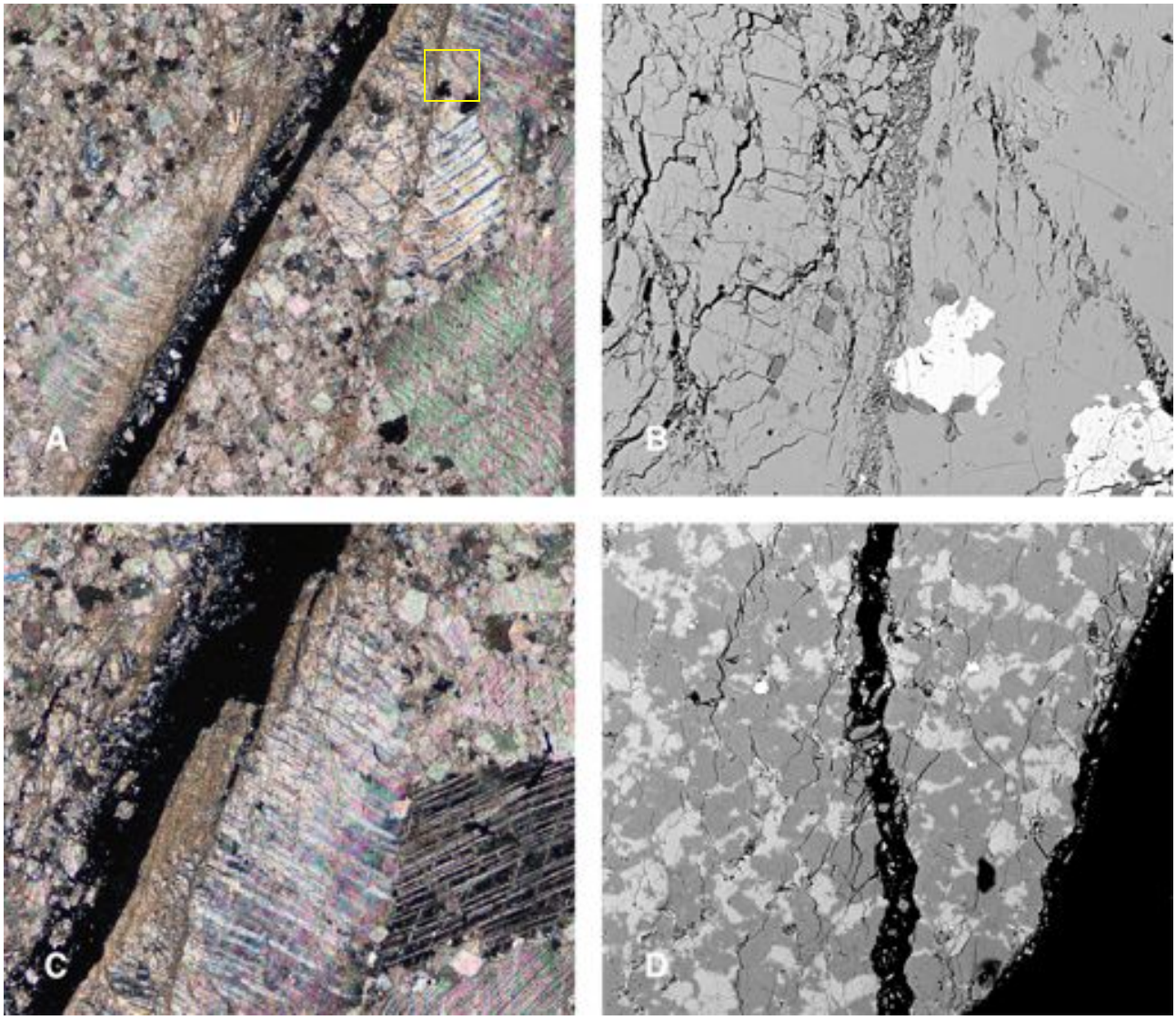

Figure 19: Exploitation of cleavage by fracture propagation in the Loomis Member 43%. *In each SEM backscatter image the dark grey matter is dolomite, the light grey is calcite and black represents voids from fracture or porosity.* **A** *Optical micrograph (XPL). Width of view* = 1.5mm. The shear rupture propagated perpendicular to the twin orientation in the lower left grain causing extensively distributed strain and disaggregation. Subsidiary fractures exploit cleavage intersections in middle right grain. The inset yellow box (top right) is the location of **B**. **B** *SEM backscatter image. Width of view* = 220μm. Fractures in calcite exploit cleavage disaggregating the grain into semi-angular shapes. Dolomite grains in the larger calcite grains enhance fracture nucleation. **C** *Optical micrograph (XPL). Width of view* = 1.5mm. Mode I cracks form in the large calcite grains prior to offset. The grain shown has been heavily comminuted as the rupture passed through perpendicular to the twin orientation. **D** *SEM backscatter image. Width of view* = 450μm. Distributed Mode I cracks isolated in the dolomite content at this composition.

material tends to intergranularly crack and disaggregate. Grain boundaries between euhedral replacement dolomite crystals and the surrounding calcite typically fracture near the damage zone (Figure 19 B). Irregular grain boundaries from poorly developed anhedral dolomite grains remain intact.

Calcite cleavage and twin planes are heavily exploited by propagating fractures in deformed Loomis Member 43%. Fractures propagate perpendicular to calcite twin orientations and cause extensive damage and disaggregation (Figures 19 A, B and C). Cleavage intersections are also exploited (Figure 19 A, grain at upper-right). Vertical fractures coalesce through dolomite networks and commonly encounter calcite grains in their propagation path (Figure 20). Strain distributes widely in intragranular fractures in the calcite grains, deterring through-going failure surface. Strain localizes in tight bands in the dolomite distributes through the vertical cleavage as narrowly spaced Mode I fractures (Figure 20 A). Finer scale fracture spacing is created towards the center of grains (Figure 20 C) in subdivisions of twin spacing. Small amounts of slip along cleavage inside large deformed calcite grain bends and shifts spaced Mode I fractures (and the columns of calcite between) slightly along the different cleavage orientation (Figure 20 B).

Strain partitioning between calcite and dolomite was variable in the Loomis Member 43% deformed samples. When a connected network exists the dolomite tends to be more deformed than the surrounding matrix. At low confining pressures the larger calcite grains proximal to the damage zone underwent extensive brittle deformation. At higher confining pressures dolomite is extensively deformed by transgranular Mode I (Figure 19 D). Offset, distributed, sub-vertical intragranular cracks were observed in many large calcite grains (Figure 19) C). Subsidiary fractures outside the main rupture zone are typically sub-vertically orientated through dolomite concentrations. Fractures dissipated and commonly reorient to favourable shear angles when propagating through concentrations of calcite. Localized discrete fracture surfaces in dolomite distribute into fracture networks in calcite when fractures propagate across grain boundaries (Figures 21 A and B). Fractures also commonly halt after propagating short distances into large calcite grains (Figure

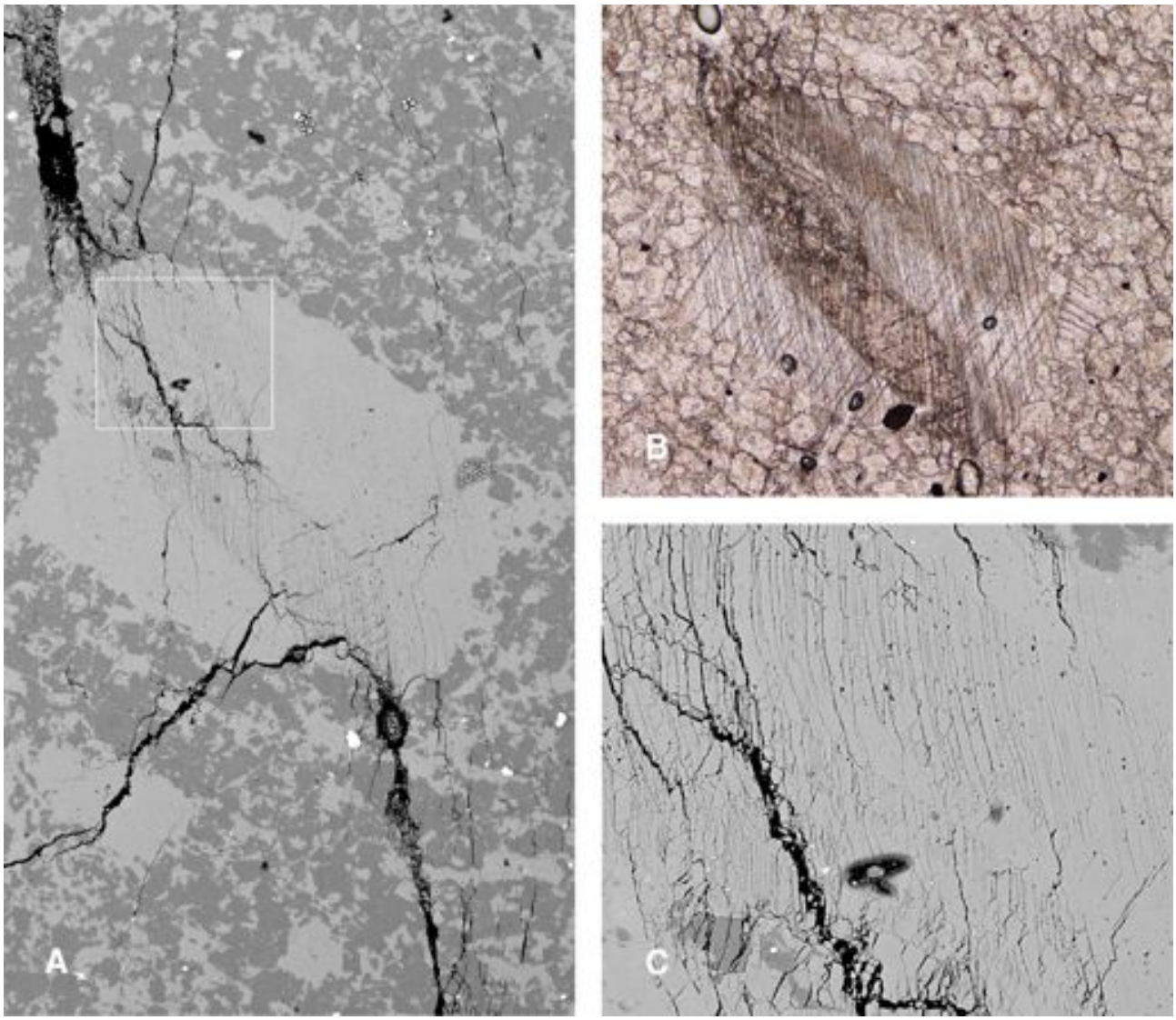

Figure 20: Strain distribution between dolomite and calcite in Loomis Member 43% **A** *All are SEM backscatter images. In each SEM backscatter image the dark grey matter is dolomite, the light grey is calcite and black represents voids from fracture or porosity. Width of view* = $1mm$. Sub-vertical fractures through dolomite dissipate into a larger calcite grain. The distributed strain causes vertical fractures to open parallel to the sub-vertical twin orientation. The inset box defines the location of **C**. **B** *Width of view* = $1mm$. *Optical micrograph (PPL).* Optical view of the grain in **A**. **C** *SEM backscatter image. Width of view* = $200\mu m$. Small amounts of bending and shifting of the segments between the spaced fractures occur in bands. The fracture spacing grades finer towards the bottom in three sub-horizontal bands.

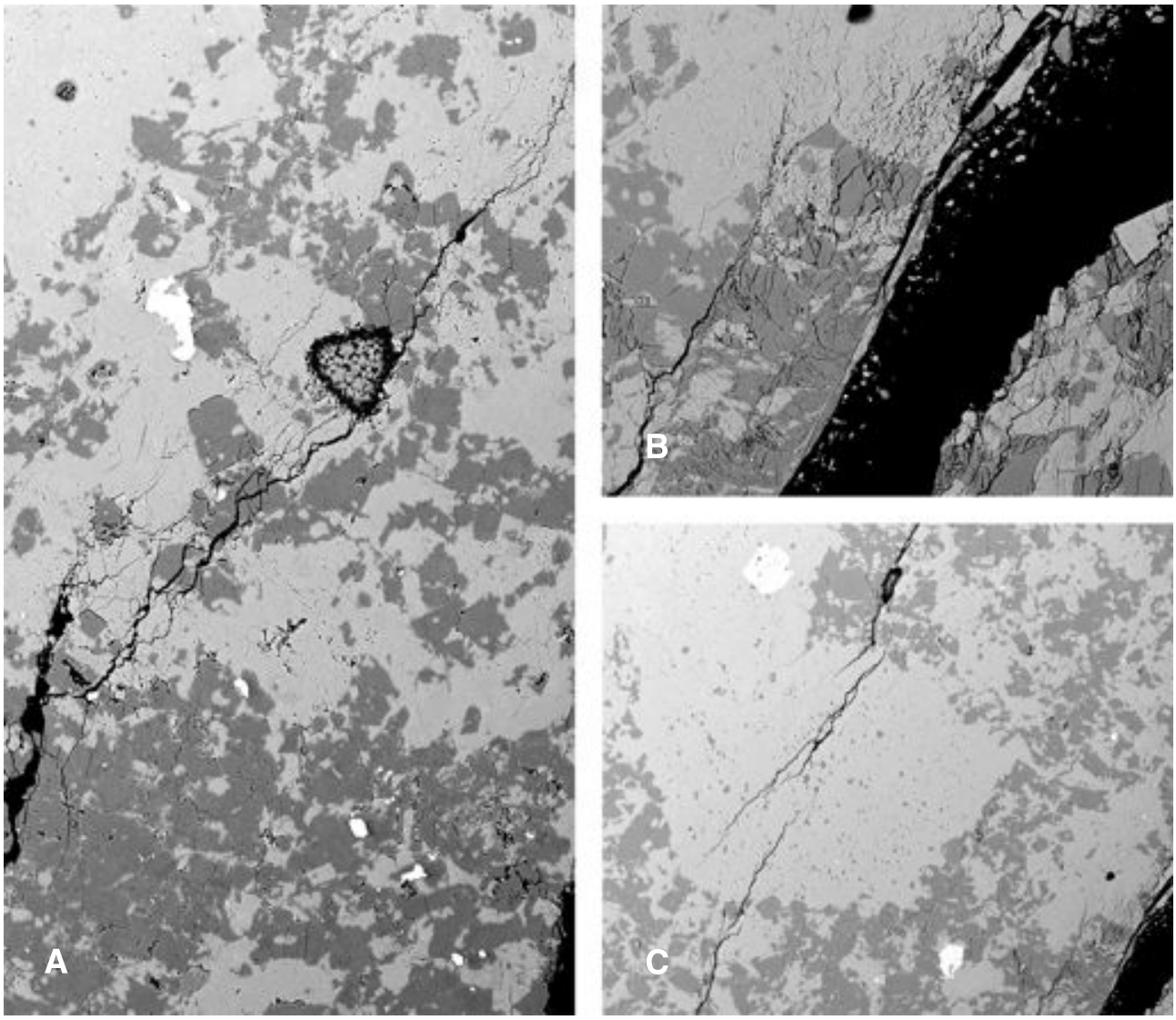

Figure 21: Fracture energy dissipation into calcite in Loomis Member 43%. *All are SEM backscatter images. In each SEM backscatter image the dark grey matter is dolomite, the light grey is calcite and black represents voids from fracture or porosity.* **A** *Width of view* $= 500\mu m$. A larger sub-vertical crack changes orientation to weave through calcite causing distributed strain. **B** *Width of view* $= 370\mu m$. Fracture surfaces are discrete in the dolomite and very distributed in the calcite.**C** *Width of view* $= 1mm$. Sub-vertical fractures halt propagation a short distance into a calcite grain. A transgranular crack formed to accommodate the deformation.

21 C).

5.5 Deformation of Baril-Wileman Member 83%

Large pathways of interconnected dolomite aid in offsetting the weakening effects of the present porosity. In volumes nearly entirely composed of dolomite the damage zone can be wide and extensively comminuted presumably due to the high order of elastic strain energy built up before release during rupture (Figures 22 C and D). The size distribution of dolomite comminution is heavily weighted towards the very fine particle size. In comparison with previous experiments discussed, calcite was not sufficiently abundant to mitigate the grain size reduction in dolomite. Figure 22 D demonstrates the mitigating effect of contiguous calcite. The upper-left portion of the footwall shows very fine comminution in dolomite. Towards the center the damage zone spreads through a calcite grain dissipating energy in the weak mineral. There is a sharp change towards the bottom dolomite, grading across the grain boundary into transgranular cracking and disaggregation of the dolomite. Intergranular cracks occur at the edges of the damage zone. Transgranular cracks through dolomite grains are generally restricted to the damage zone and uncommonly occur along cleavage orientations. Most fragments of broken dolomite and comminuted particles are irregularly shaped.

Dolomite replacement textures are more common at this composition both as mineral growth in centers of calcite grains(Figure 22 B) and as growth into calcite grains from the grain boundaries (Figure 22 A). Fracture networks concentrate inside grains affected by dolomite replacement (Figure 22 A). Impinging dolomite grains commonly create fine-scale deformation twinning in calcite (Figure 23 C).

Twin planes and cleavage are commonly exploited at this composition. The majority of the calcite content is restricted to larger twinned grains. Favourably oriented grains act as modifiers to the fracture path to further realize shear failure angles (Figures 23 A and B). Mineral strength determines the effective fracture spacing. Fractures in calcite space closer together than fractures

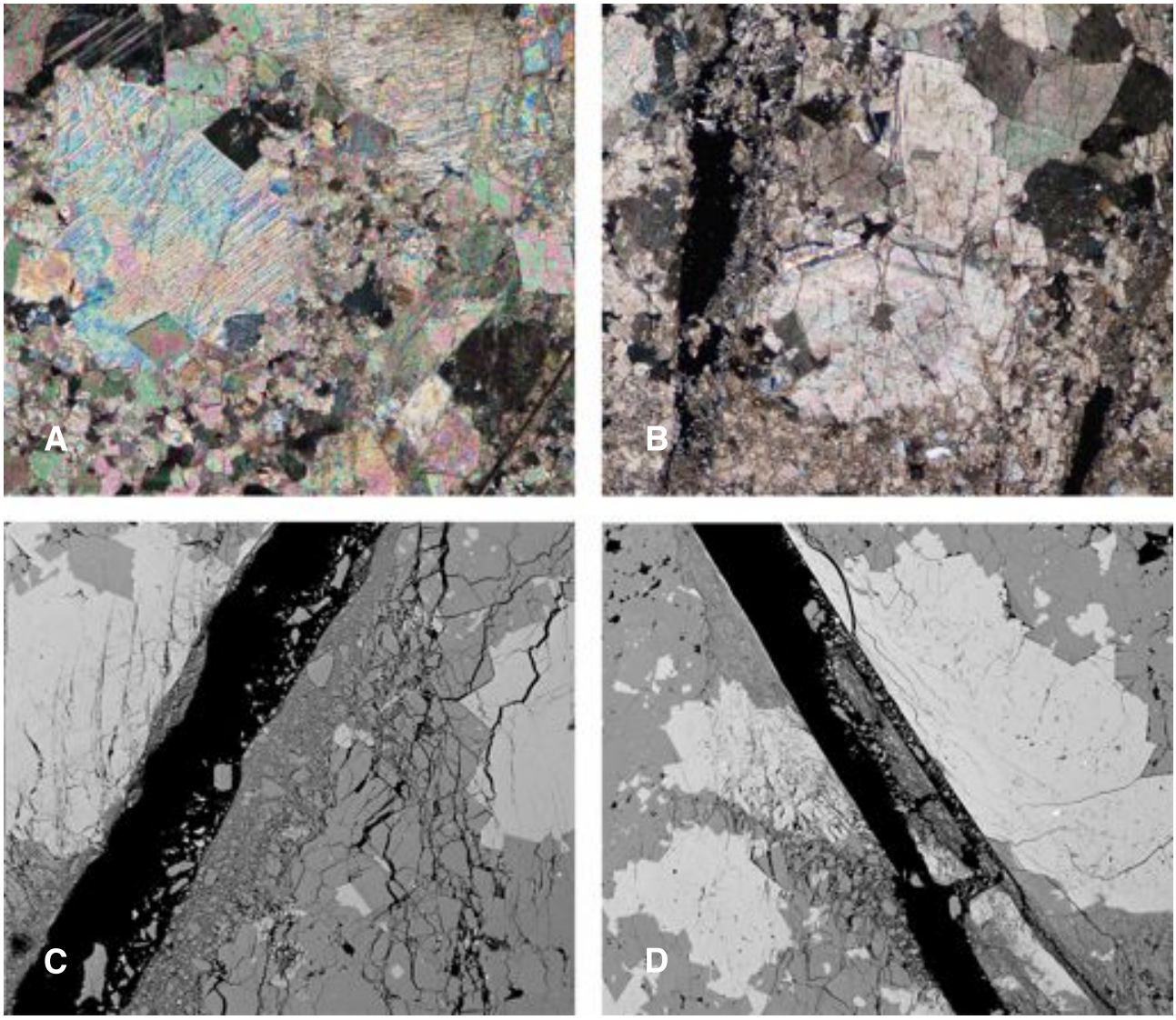

Figure 22: Comminution and the effects of replacement textures in Baril-Wileman Member 83%. *In each SEM backscatter image the dark grey matter is dolomite, the light grey is calcite and black represents voids from fracture or porosity.* **A** *Optical micrograph (XPL). Width of view* = 750μm. Fracture concentrated in calcite grains where dolomite crystals formed at the grain boundary. **B** *Optical micrograph (XPL). Width of view = 1.5mm* Fracture concentrated in calcite grains where dolomite crystals formed in the center of the calcite grain. **C** *SEM backscatter image. Width of view* = 550μm. Comminution in dolomite showing angular, irregular grains with a large distribution of sizes. In the upper left a calcite crystal shows vertical fractures that opened exploiting cleavage and that were bent during failure displacement. **D** *SEM backscatter image. Width of view = 1.1mm* Comminution of the footwall exhibits a very fine particle size at the top left that increases in size distribution through the calcite grain and grades into transgranular cracks and disaggregation across the grain boundary into the dolomite at the bottom.

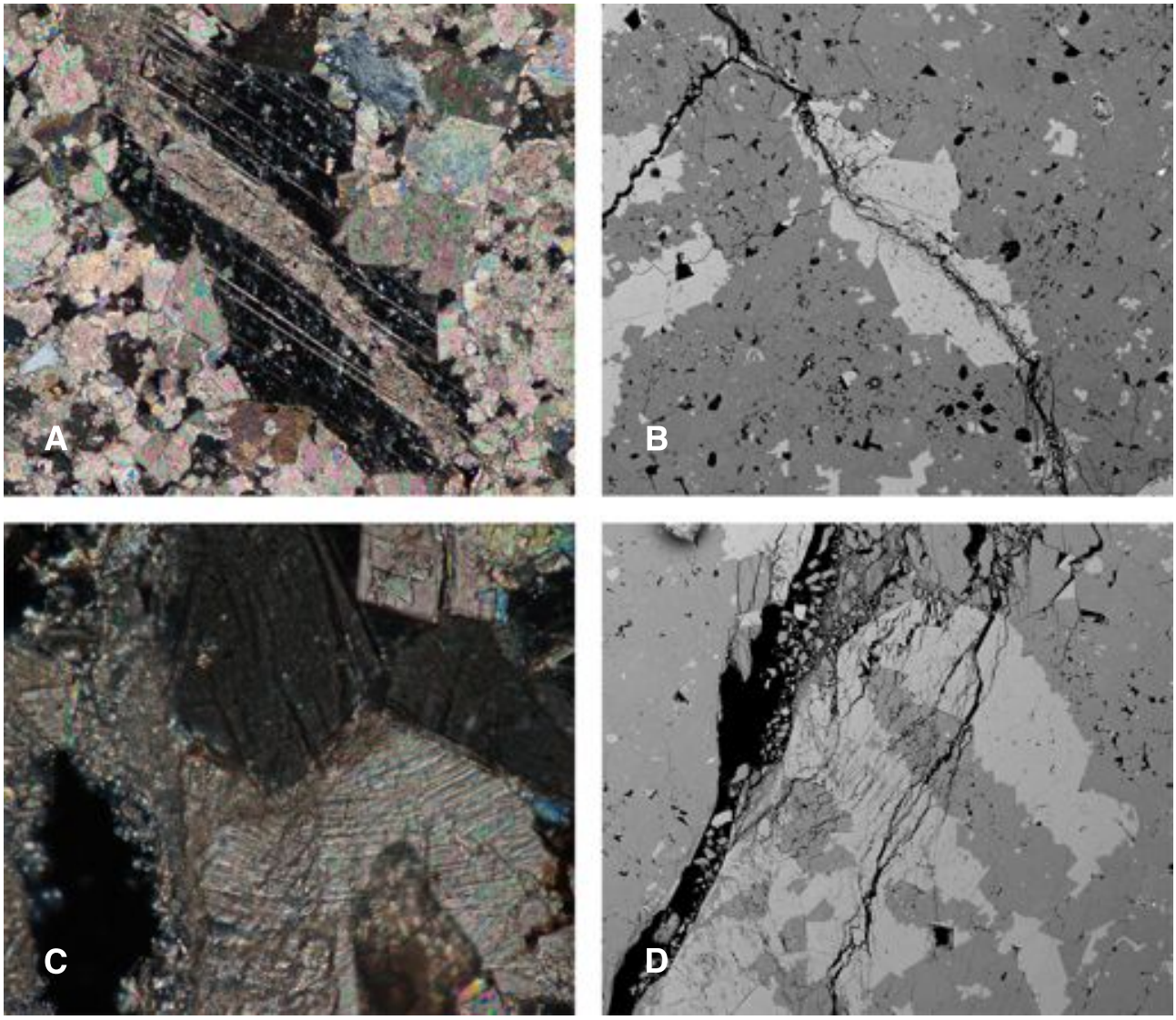

Figure 23: Exploitation of cleavage by fractures in Baril-Wileman Member 83%. *In each SEM backscatter image the dark grey matter is dolomite, the light grey is calcite and black represents voids from fracture or porosity.* **A** *Optical micrograph (XPL). Width of view* = 750μm. Sub-vertical fractures propagating through dolomite exploit the weak twin planes and create a wide damage zone throughout the center calcite grain. **B** *SEM backscatter image. Width of view = 1mm.* This is an image of the same grain as in **A**, showing the dolomite distribution in darker grey. **C** *Optical micrograph (XPL). Width of view* = 300μm. A dolomite grain impinging on calcite created fine-scale deformation twinning in a calcite grain. **D** *SEM backscatter image. Width of view = 1.1mm* Fracture spacing is closer in the calcite material. In the dolomite fractures are fewer, wider and spaced farther apart.

that propagate through contiguous dolomite (Figure 23 D). Mode I fractures develop prior to failure along sub-vertical twin planes in calcite and are offset by the displacement (Figure 22 C, upper-left). The material between such twins are commonly bent in the process of failure.

5.6 Deformation of Fairholme 'C' 99%

Fairholme 'C' was relatively weak at low confining pressures but had drastic strength increases with higher confining pressures. Similarly to the Loomis Member 43% the stylolites found in each sample may have contributed to this weakness at low confining pressures, but had reduced effects at higher confining pressures. Its large grain size may influenced its peak strengths negatively.

Shear ruptures initiated in Fairholme 'C' create wide damage zones with irregularly distributed extensive fine comminution (Figures 24 B). The wide failure zones commonly have fairly smooth walls (Figure 24 C) but the damage zone makes a sharp transition to just intergranular and intragranular cracking between and in the dolomite (Figure 24 A). Dolomite grains commonly disaggregated readily along grain boundaries and cleavages (Figure 24 D).

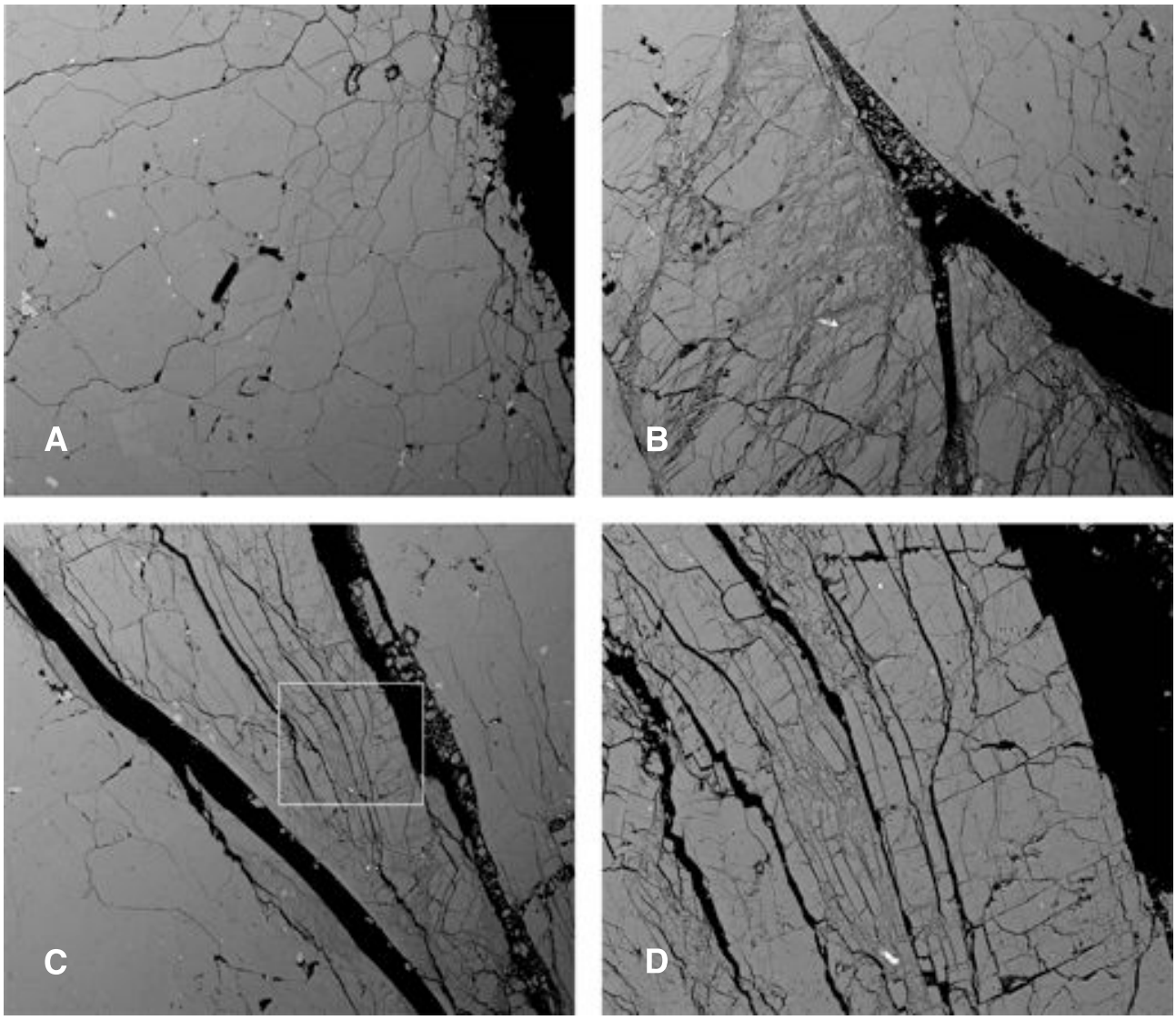

Figure 24: Deformation of Fairholme 'C' 99%. *All are SEM backscatter images. In each SEM backscatter image the dark grey matter is dolomite, the light grey is calcite and black represents voids from fracture or porosity.* **A** *Width of view* $= 1.9mm$. Intergranular cracking in dolomite throughout the damage zone. **B** *Width of view* $= 1.9mm$. Distributed strain and comminution in dolomite. Comminution is irregular and has a wide distribution of particle sizes. **C** *Width of view* $= 1.9mm$. Smooth walled failure sufaces. The inset box defines the location of **D**. **D** *Width of view* $= 450\mu m$. Dolomite fracturing along cleavage and starting to disaggregate.

6 Discussion

The experimentation in this research explored the mechanical effects of dolomite enrichment in limestone rocks under various confining pressures. Dolomite content, the inherent dolomite replacement textures and the existing grain scale structures, such as twins, largely determined and influenced failure mechanics, fracture propagation dynamics and the strength of the rocks tested. The range between 30 to 45 weight percent dolomite was a threshold of grain boundary connectivity that created load-bearing structures [7], [5], [9]. This changed the distribution of strain by localizing deformation into the younger, stronger dolomite.

6.1 Mechanical Results

Peak strengths achieved in this study have little correlation with similar materials tested by previous workers due to the different textures. The end-member sedimentary limestone (Loomis 3%) peaked at similar strengths to Carrara Marbles used by Zhang et. al. [11] even though Carrara has larger grain sizes, and existing twin lamellae. Metamorphic dolomites deformed by Austin [1] were comparably weaker than Fairholme 'C' 99%. The grain sizes of the low-porosity materials used by Austin were smaller, the rocks contained dynamically recrystallized grains devoid of imperfections, contained little to no existing structure such as stylolite solution seams as with Fairholme 'C', but the coarser grains had lobate grain boundaries. The polygonal grain boundaries of Fairholme 'C' may have been a significant contributor to this discrepancy. With distributing strain during the onset of yielding polygonal grains may be able to slip and promote intergranular fracturing instead of extensive transgranular fracturing found from lobate grain boundaries locking together [1]. The variably dolomitized samples hold few analogies to other rock deformation work reported.

6.2 The Role of Dolomite Replacement Textures

The replacement of limestone by secondary dolomite leads to highly variable texture within the rocks. The Loomis Member 3%, with low dolomite content, has large calcite grains with a significant micritic sized matrix. Small dolomite crystals that nucleated within relatively large calcite grains provide small imperfections and created sites of stress concentrations promoting fracture nucleation (Figures 15 A and B). With increasing dolomite content, dolomite replaced matrix micrite, which results in grain boundaries between dolomite and larger calcite crystals. Euhedral dolomite crystals typically create angular corners that impinged on calcite crystals concentrating stress at their points (Figure 23 C) and promote transgranular fracture propagation across the calcite grains (Figure 22 A and B). Replacement dolomite growths in the center of calcite caused thorough fracturing and breakdown of the calcite grains (Figures 18 C and D). The high dolomite content composite has calcite crystals completely encased in dolomite. Calcite grains act as sites for strain accommodation and as weak patches to dissipate elastic strain energy stored in the dolomite networks as distributed strain (Figure 20). They are also used alternatively to reorient sub-vertical fracture propagation paths into Mode III orientations (Figures 23 A and B). The enrichment of dolomite inevitably leads to higher mechanical strength of dolomite–limestone composites but the replacement textures, to a lesser degree, weaken the rock.

6.3 The Role of Cleavage and Calcite Twins

All samples, with exception of the pure dolomite sample, Fairholme 'C', contain calcite grains with twins, typically in two orientations. Calcite grains with twins are typically larger than dolomite grains. At all confining pressures, fractures exploit the weakness along twin planes and cleavages oriented in angles favouring shear, to promote displacement and macroscopic failure (Figure 16 A) [4]. Fractures that propagate between calcite grains utilize weak micritic matrix to redirect propagation to line-up with twin orientations and connect the grains (Figure 16 B).

Calcite twins oriented close to the maximum compression are typically reactivated as Mode I cracks. Higher confining pressure experiments show extensive sub-vertical cracks interpreted to be pre-failure because of visible offset (Figures 15 C and 22 C). Twin spacing controls fracture spacing by breaking only at twin boundaries or at regular subdivisions between twins (Figures 20, 23 C and D). Finer fracture or deformation twin spacing implies higher stress concentration [6]. In many grains closely divided lengths of twins broke apart in an opposing orientation as well causing disaggregation of heavily damaged grains (Figure 16 C). The few occurrences of dolomite exhibiting fracture cleavage were from high confining pressure deformation of Fairholme 'C' (Figure 24 D). In composite limestones the presence of calcite in the system must deter the buildup of elastic strain energy to the point that, during failure, would shock the dolomite into distributing strain evenly amongst cleavage. The breakdown of dolomite along its cleavage orientations in Figure 24 D is an analog to the disaggregation and grain size reduction seen in calcite grains throughout the experimental suite. Thus, overall, the role of pre-existing cleavage is to reduce the strength of the rock.

6.4 Dolomite Grain Support Networks

Increasing dolomite content in the rocks increases interconnectivity between dolomite grains. Single phase grain support networks in the two phase system tend to localize strain during failure [2],[7]. Below the threshold of an interconnected dolomite support network (30-45% dolomite) the calcite absorbs the majority of the elastic strain energy applied. This is noted by the fracture networks confined to purely calcite paths (Figure 17). This means the majority of the strain energy released to maintain fracture propagation was stored in calcite, the load-bearing network at this composition. Minor stress buildup in dolomite may contribute small portions of the fracture energy when fracture tips exploit weak grain boundaries between calcite and dolomite. Above the threshold (eg. Loomis 34%) deformation abruptly shifts into the dolomite material. Therefore, a threshold of dolomite connectivity is required to appreciably increase the strength of the rock.

This is similar to what is observed in clay gouges with quartz. A threshold percent of quartz is required in the clay gouge to appreciably increase the strength of the gouge material [7]. The specific distribution of grains in the Loomis Member 34% with larger calcite grains restricts the space containing dolomite and greatly enhances the connectivity to the network. The Salter Member 31% has no such network and exhibits strain distribution into the calcite phase (Figure 17). In many samples with medium dolomite compositions, failure that initiates from stressed dolomite networks deviates from the network through calcite material to suit the favourable shear orientation. The calcite, with less built-up elastic strain energy, dissipates fracture energy by splaying the fracture tip causing distributed damage inside the grains (Figure 21). In higher dolomite content rocks, calcite grains encased by dolomite grains generally show extensive development of Mode I cracks. The Mode I cracks may have had two effects: 1) Dolomite accommodated strain in the sample and allowed the system of dolomite grains to compress further, enhancing the contact between dolomite grains and hence the support system. 2) The large Mode I fractures caused a site for the initiation of shear rupture, or attracted fractures propagating through the dolomite network. Increased confining pressure deters the propagation of the Mode I fractures and enhance ductile strain accomodation.

6.5 Natural Heterogeneity of Limestone-Dolomite Composites

This research has produced data and analyses specific to a unique set of rocks. Further experimentation with a variety of other dolomite compositions with differing grain sizes and textures would elucidate more general judgement on the mechanisms of failure in variably dolomitized limestones. A statistical approach to experiments would help quantify and accurately characterize the mechanical data so as to provide specific correlation to the textural analyses. Previous work of Zhang et. al. [11] deformed synthetic calcite aggregates to compare to the results from the natural Carrara Marble. The results yielded peak stresses much higher than the natural samples although grain size was smaller. Creating synthetic aggregates of variable dolomite content in

limestone could provide a useful set of gauges to compare to the deformation of natural limestones and highlight the nature of the role of texture on strength. Establishing the content required to reach the threshold of interconnectivity of dolomite grains in a sample with an even grain size and similar grain sizes between the two constituents would be valuable for comparison to naturally occurring grain distributions.

7 Conclusion

A threshold exists for the content of dolomite that is required to significantly increase the strength of limestones. This support network, which represents the amount of dolomite needed to create a load bearing network, emerged in the 31 to 43% dolomite range. The support network enabled the rock to absorb and partition elastic strain differently between dolomite and calcite. The enrichment of dolomite in limestone rock samples produces an effective increase in the structural capacity of the rock to compress and store, and then release, during failure, elastic strain energy creating extensive fine comminution in the damaged shear zones. Below this apparent threshold the dolomite is dispersed and does not effectively increase the strength of the rock: the calcite effectively is the load bearing network. The internal structure to grains provided many opportunities for deformation to actively exploit textures of weakness such as twin planes, grain boundaries and replacement dolomite inclusions, especially in larger calcite grains. Cleaner and more regular grain boundaries provide structure in higher dolomite contents that translates to a larger strength response from increasing confining pressure. The experimental suite realized a 397 MPa range to the peak strengths. The mechanical data produced provides a set of gauges for the behaviour of variably dolomitized limestones under stress in the brittle regime of the crust.

8 Tables

Sample	Rock Type	Mass(g)	Diam.(mm)	Length(mm)	Porosity(%)	Density ($\frac{g}{cm^3}$)
07-NC-07	MHL 3%	110.72	29.53	60.11	0.84	2.713
07-NC-17	MHL 3%	112.33	29.75	60.05	0.50	2.704
07-NC-25	MHL 3%	111.77	29.64	60.03	0.10	2.702
07-NC-34	Salter 31%	114.69	29.81	60.22	0.19	2.733
07-NC-18	Salter 31%	113.89	29.63	59.99	-0.71	2.735
07-NC-26	Salter 31%	114.48	29.82	60.10	0.34	2.737
07-NC-16	MHL 34%	115.09	29.84	60.01	0.43	2.754
07-NC-13	MHL 34%	115.71	29.89	60.02	0.52	2.762
07-NC-39	MHL 34%	115.12	29.83	60.00	–	–
07-NC-11	MHL 43%	114.59	29.78	59.77	–	–
07-NC-19	MHL 43%	115.33	29.85	60.13	0.41	2.752
07-NC-38	MHL 43%	115.41	29.76	60.12	–	–
07-NC-06	Opal 48%	114.59	29.76	59.97	0.31	2.756
07-NC-29	Opal 48%	114.19	29.60	59.81	0.42	2.750
07-NC-40	Opal 48%	114.60	29.75	60.06	–	–
07-NC-14	BW 83%	114.42	29.78	60.05	3.10	2.823
07-NC-35	BW 83%	114.66	29.80	60.08	3.29	2.830
07-NC-41	BW 83%	114.23	29.78	60.06	3.56	2.831
07-NC-15	Alevo 94%	112.32	29.82	60.04	6.08	2.853
07-NC-22	Alevo 94%	111.45	29.82	60.00	7.01	2.860
07-NC-32	Alevo 94%	111.92	29.81	59.99	6.40	2.857
07-NC-42	FairC 99%	118.07	29.84	60.05	1.53	2.855
07-NC-23	FairC 99%	118.24	29.84	60.12	1.46	2.854
07-NC-37	FairC 99%	118.33	29.85	60.03	1.53	2.861

Table 1: Pre-deformation Sample Measurements. The mass, diameter and length were measured manually. Porosity and density are calculated results of pycnometry.

Sample	Rock Type	P_c	Pk Str (MPa)	Failure ε %	Angle	Offset(mm)	ϕ (%)	Response	Young's Modulus
07-NC-07	MHL 3%	25	306.4	0.96	21	1.0	0.84	Positive	582.1
07-NC-17	MHL 3%	50	360.0	1.17	21	0.8	0.50	Positive	510.0
07-NC-25	MHL 3%	75	376.7	1.00	23	0.95	0.10	Negative	529.4
07-NC-34	Salter 31%	25	422.2	0.76	14	1.4	0.19	Negative	1013.3
07-NC-18	Salter 31%	50	448.8	1.3	17	1.2	-0.70	Negative	589.0
07-NC-26	Salter 31%	75	516.3	2.74	22	0.6	0.34	Negative	597.0
07-NC-16	MHL 34%	25	402.8	1.17	25	1.4	0.43	Positive	637.9
07-NC-13	MHL 34%	50	498.2	1.2	30	1.0	0.52	Positive	637.1
07-NC-39	MHL 34%	75	569.3	1.45	–	–	0.43	Negative	1043.3
07-NC-11	MHL 43%	25	337.8	1.2	17	0.7	0.33	Negative	526.6
07-NC-19	MHL 43%	50	437.7	1.3	23	1.3	0.41	Positive	568.0
07-NC-38	MHL 43%	75	522.4	1.02	–	–	0.32	Negative	875.3
07-NC-06	Opal 48%	25	526.5	1.28	20	2.0	0.305	Positive	654.9
07-NC-29	Opal 48%	50	566.3	0.95	8	1.4	0.42	Negative	741.3
07-NC-40	Opal 48%	75	676.1	0.85	–	–	0.35	Negative	1234.8
07-NC-14	BW 83%	25	394.9	1.38	20	1.6	3.10	Negative	536.4
07-NC-35	BW 83%	50	541.4	0.75	–	–	3.30	Positive	810.4
07-NC-41	BW 83%	75	643.4	1.01	–	–	3.56	Negative	970.9
07-NC-15	Alevo 94%	25	360.2	1.28	29	1.1	6.1	Negative	505.3
07-NC-22	Alevo 94%	50	406.2	1.09	32	2.2	7.01	Negative	523.5
07-NC-32	Alevo 94%	75	439.7	1.02	32	1.1	6.4	Positive	619.2
07-NC-42	FairC 99%	25	473.0	0.65	–	–	1.53	Negative	1040.2
07-NC-23	FairC 99%	50	574.1	1.19	27	1.2	1.5	Negative	799.3
07-NC-37	FairC 99%	75	703.1	0.82	–	–	1.5	Positive	1603.4

Table 2: Collection of measurements from deformed samples and calculations from reduced data. *Angle* refers to the angle of the failure plane from σ_1. *Offset* refers to the offset between the hanging wall and footwall produced by the rupture. ϕ is the porosity. *Response* refers to the response of Poisson's Ratio to σ_d (See Figure (FIGURE)).

Rock Type	Avg Porosity(%)	Std Dev	Avg Density ($\frac{g}{cm^3}$)	Std Dev
MHL 3%	0.463	0.217	2.7051	0.0030
Salter 31%	0.156	0.387	2.7338	0.0021
MHL 34%	0.440	0.153	2.7518	0.0077
MHL 43%	0.329	0.112	2.7548	0.0042
Opal 48%	0.356	0.082	2.7560	0.0069
BW 83%	3.414	0.306	2.8289	0.0055
Alevo 94%	6.302	0.528	2.8546	0.0037
FairC 99%	1.558	0.229	2.8567	0.0021

Table 3: Statistical calculations based off of all undeformed samples cored for each rock type sampled.

Rock Type	Calcite %	Dolomite %	Silica %
MHL 3%	95.71	3.15	1.14
Salter 31%	63.59	31.17	5.24
MHL 34%	61.09	34.36	4.55
MHL 43%	48.14	43.30	8.56
Opal 48%	38.47	47.87	13.66
BW 83%	14.72	83.48	1.80
Alevo 94%	3.73	93.98	2.29
FairC 99%	0.62	98.60	0.78

Table 4: Mineral percentages calculated from XRF oxide weight-percent data (APPENDIX) and normalized to one-hundred percent.

Rock Type	Avg Grain Size (mm)	Std Dev	Max Size (mm)	Min Size (mm)
MHL 3%	0.318	0.301	2.156	0.049
Salter 31%	0.052	0.047	0.272	0.010
MHL 34%	0.078	0.108	0.784	0.010
MHL 43%	0.045	0.069	0.594	0.005
Opal 48%	0.027	0.014	0.079	0.005
BW 83%	0.062	0.055	0.248	0.005
Alevo 94%	0.155	0.085	0.412	0.020
FairC 99%	0.198	0.127	0.608	0.020

Table 5: Grain size distribution statistics calculated using counts of one-hundred grains from thin-section observations. Thin-sections were from undeformed protolith samples and may not represent the entire range of grain sizes seen in deformed samples. The minimum size does not include the micrite portion of the sample.

Rock Type	$\tau = C + \mu \times \sigma_n$	θ_α	θ_β
MHL 3%	$\tau = 89.1 + 0.448 \times \sigma_n$	$60.6\,^\circ$	$52.3\,^\circ$
Salter 31%	$\tau = 106.2 + 0.549 \times \sigma_n$	$55.2\,^\circ$	$62.5\,^\circ$
MHL 34%	$\tau = 78.1 + 0.799 \times \sigma_n$	$65.5\,^\circ$	$63.0\,^\circ$
MHL 43%	$\tau = 57.5 + 0.852 \times \sigma_n$	$65.9\,^\circ$	$64.5\,^\circ$
Opal 48%	$\tau = 106.5 + 0.738 \times \sigma_n$	$58.2\,^\circ$	$66.7\,^\circ$
BW 83%	$\tau = 57.5 + 1.014 \times \sigma_n$	$69.1\,^\circ$	$66.1\,^\circ$
Alevo 94%	$\tau = 100.4 + 0.493 \times \sigma_n$	$59.3\,^\circ$	$56.8\,^\circ$
FairC 99%	$\tau = 74.1 + 0.971 \times \sigma_n$	$66.0\,^\circ$	$68.1\,^\circ$

Table 6: Coulomb failure criteria calculated from Mohr diagrams. The functions define the internal cohesion (C) and the coefficient of internal friction (μ). θ_α and θ_β refer to the theoretical angle of the failure plane (Norm to failure plane is $\theta\,^\circ$ from σ_1) for the first and second pairs of circles, respectively ($P_c = 25, 50$ MPa and $P_c = 50, 75$ MPa).

9 Appendix

9.1 X-Ray Fluorescence Data

The XRF data was provided by ALS Chemex of North Vancouver, British Columbia. Major element and trace element oxide percents were provided. Table 7 summarizes the results. To produce the calculated values stated in Table 4 the carbon dioxide lost on ignition was needed to be recombined with the oxides. The formulae for calcite and dolomite, respectively are $CaCO_3$ and $CaMg(CO_3)_2$ and the system represented by the data was noticed to mainly involve calcite, dolomite, and silica. The weight percents of all MgO data were converted into moles, assuming a one-hundred gram sample, by dividing by the molecular weight. With the number of moles known the number of moles of dolomite are the same assuming dolomite was the only magnesian mineral present. Converting the weight percents of all CaO data into moles, by dividing by its molecular weight, then subtracting the calculated number of moles of dolomite gives a remainder of CaO to make calcite. The numbers of moles of dolomite and calcite yield the weights of each mineral present in the assumed one-hundred gram sample. Ignoring all the other oxide percents and to consider the system as the simple ternary system with Silica, Calcite and Dolomite the calculated were normalized to 100% and expressed in Table 4.

9.2 Data Reduction

Each data set produced from an experiment was reduced in size to contain only the relevant portion of the differential stress load applied until failure. A Matlab program was developed that calculated the gradients between displacement data which was subsequently smoothed with a moving average. Each datum above a threshold just under the known displacement rate was flagged to isolate the subset of the data where the load was initiated, after confining pressure had been applied, to the moment of failure. Displacement was halted immediately after failure preventing further data from being flagged. The Labview Virtual Instrument program developed

Sample Type	SiO_2 %	Al_2O_3 %	Fe_2O_3 %	CaO %	MgO %	Na_2O %	K_2O %	Cr_2O_3 %	TiO_2 %	P_2O_5 %	SrO %	LOI %	Total %
MHL 3%	1.11	0.06	0.05	53.08	0.67	0.01	0.02	0.01	<0.01	0.015	0.02	43.4	98.45
Salter 31%	5.05	0.37	0.30	43.52	6.57	0.04	0.11	0.01	0.01	0.045	0.02	42.1	98.15
MHL 34%	4.37	0.61	0.31	42.97	7.22	0.06	0.12	<0.01	0.02	0.017	0.01	42.5	98.22
MHL 43%	8.15	1.42	0.45	38.23	9.01	0.11	0.28	<0.01	0.08	0.035	0.01	40.5	98.29
Opal 48%	12.74	2.25	0.37	33.7	9.76	0.15	0.62	<0.01	0.1	0.029	0.02	38.4	98.15
BW 83%	1.75	0.18	0.07	32.77	17.77	<0.01	0.09	<0.01	<0.01	0.065	0.01	45.5	98.2
Alevo 94%	2.22	0.24	0.08	29.77	19.93	0.01	0.05	<0.01	0.01	0.011	0.01	46	98.34
FairC 99%	0.76	0.27	0.13	29.47	20.93	<0.01	0.06	0.01	<0.01	0.007	0.01	46.7	98.34

Table 7: XRF Percent-Oxide Data. BaO and MnO were also present in amounts <0.01%.

previously for utilizing the LSR records seven fields of data relevant to this experimental suite. The date and time are recorded in two separate fields. The displacement is recorded in inches, accurate to seven decimal points, from the external displacement transducer. The confining pressure is recorded in Megapascals from the pressure transducer placed in the line between the gas booster and the pressure vessel. The load is measured by the load cell and recorded in units of pounds of force. Two separate fields record the data reported from the two strain gauges, one in the axial orientation, the other in the transverse. The strain gauge data is reported in strain, a dimensionless number representing the ratio of the initial length of the dimension to the deformed length.

Also recorded by the Labview program, but not of direct application to the experimental data, were pore-fluid pressures from the upper and lower pore pressure transducers. No fluids were intentionally applied in the pore-fluid system during any of the experiments in this suite but setting up the pore-fluid system for the pressure transducers to be able to collect pore-fluid pressure readings proved useful for quality control of the experiments. Occasionally, due to deterioration of the o-rings on each of the pistons preventing leakage of the confining medium between the piston and the piston cup, leaks into the sample did occur. This could be detected with the pore-fluid pressure transducers and such experiments were halted and the o-rings changed to prevent such leakage.

After isolating the relevant data, the following formulae were applied to produce the data forms depicted in this publication. The displacement was converted from inches to millimeters, and the initial reading was subtracted from each datum to set the inital reading to zero:

$$true\ displacement\ (mm) = (displacement\ (inches) - displacement_{initial}) \times 25.4\ \frac{mm}{inch}$$

The load, in pounds, was converted to load in kilograms, and the initial reading was subtracted from each datum to set the initial reading to zero:

$$true\ load\ (kg) = (load\ (lbs) - load_{initial}) \times 0.4535924\ \frac{kg}{lb}$$

Percent-strain was calculated from the displacement data, modified by applying a load-dependent stiffness variable. The stiffness factor, dependent on confining pressure, was calculated according to the linear equation:

$$Stiffness\ Factor = 285570.4 + 565.4 \times P_c$$

As the confining pressure remained constant throughout the experiment one stiffness factor was used for all the reduced data. The stiffness factor represent a load dependent variable that gauges how much elastic energy and hence displacement is being absorbed by the apparatus itself instead of the rock sample. The equation for the stiffness factor was interpolated from calibration measurements made for larger and smaller diameter samples by Nick Austin [1]. The calibration performed involved elastically deforming H13 hardened steel cylinders with an independently measured Young's Modulus. The stiffness factor used in context allowed the calculation of percent-strain:

$$Strain(\%) = \frac{true\ displacement \times \frac{1cm}{10mm} - true\ load \times \frac{1}{stiffnessfactor}}{original\ length\ of\ core\ sample\ (cm)} \times 100\%$$

With the strain calculated the stress was then able to be calculated. With stress being $\frac{force}{area}$ during an experiment the strain was assumed to affect the dimensions of the core sample and hence the stress state. Using the original cross-sectional area of each core sample and the strain at each datum, the following calculation was performed to provide the stress in $\frac{kg}{cm^2}$, a stress state assumed to be kilograms of force acting under the acceleration due to gravity:

$$Stress\ \left(\frac{kg}{cm^2}\right) = \frac{load\ (kg)}{Core\ Area\ (cm^2) \times \left(1 + \frac{Strain(\%)}{100\%}\right)}$$

Furthermore the stress in $\frac{kg}{cm^2}$ was converted to stress in Megapascals, by factoring in the acceleration due to gravity and scaling the order:

$$Stress\ (MPa) = Stress\ \left(\frac{kg}{cm^2}\right) \times \frac{10\,000\ cm^2}{1\ m^2} \times 9.80665\ \frac{m}{s^2} \times \frac{1\ MPa}{1\,000\,000\ Pa}$$

The strain measurements from the strain gauges was converted to percent-strain by multiplying by 100%. Poisson's ratio (ν) was calculated from the transverse and axial strain supplied by the gauges:

$$\nu = -\frac{\varepsilon_{trans}}{\varepsilon_{axial}}$$

References

[1] Austin, N.J., 2003. An experimental investigation of textural controls on the brittle deformation of dolomite. *Masters of Science Thesis, University of British Columbia*, 95 pp.

[2] Barhoorn, A., Bystricky, M., Kunze, K., Burlin, L., 2005. Strain localization in bimineralic rocks: Experimental deformation of synthetic calcite-anhydrite aggregates. *Earth and Planetary Science Letters*, 240: 748-763.

[3] Baud, P., Schubnel, A., Wong, T.F., 2000. Dilatancy, compaction, and failure mode in Solnhofen limestone. *Journal of Geophysical Research*, 105, B8 :19289-19303.

[4] De Bresser, J.H.P., Spiers, C.J., 1997. Strength characteristics of the r, f, and c slip systems in calcite. *Tectonophysics*, 272: 1-23.

[5] Giger, S.B., 2007. Permeability and strength evolution of quartz fault gouges at hydrothermal conditions. *Ph.D. Thesis, Australian National University*, 125 pp.

[6] Lacombe, O., Laurent, P., 1992. Determination of principal stress magnitudes using calcite twins and rock mechanics data. *Tectonophysics*, 202: 83-93.

[7] Logan, J.M., Rauenzahn, K.A., 1987. Frictional dependence of gouge mixtures of quartz and montmorillonite on velocity, composition and fabric. *Tectonophysics*, 144: 87-108.

[8] Palchik, V., Hatzor, Y.H., 2000. Correlation between mechanical strength and microstructural parameters of dolomites and limestones in the Judea Group – Israel. *Israel Journal of Earth Sciences*, 49, 2: 65-79.

[9] Roessig, K.M., Foster, J.C., Jr., Bardenhagen, S.G., 2002. Dynamic stress chain formation in a two-dimensional particle bed. *Experimental Mechanics*: 329-337.

[10] Weiss, L.E., Turner, F.J., 1972. Some observations of translation gliding and kinking in experimentally deformed calcite and dolomite. *Flow and fracture of rocks, the Griggs volume, American Geophysical Union*, p 352.

[11] Zhang, S., Cox, S.F., Paterson, M.S., 1994. The influence of room temperature deformation on porosity and permeability in calcite aggregates. *Journal of Geophysical Research*, 99, B8: 15,761 - 15,775.